

Investigating the Conformational Dynamics of Biomolecules using Optical
Tweezers

by

JingChyuan Soong

A thesis submitted in partial fulfillment of the requirements for the degree of

Master of Science

Department of Physics
University of Alberta

© JingChyuan Soong, 2014

Abstract

The structural dynamics of proteins and nucleic acids play a vital role in biochemical reactions. We employed novel optical tweezers to study the programmed -1 ribosomal frameshifting, where the conformational plasticity of a SARS pseudoknot with a bound ligand is shown to be correlated to the frameshifting efficiency. We also investigated a mechanical model for components involved in optical tweezers, and tested their validity through a series of measurements.

Preface

Chapter 3 of this thesis has been published as Dustin B. Ritchie, Jingchuan Soong, William K. A. Sikkema, and Michael T. Woodside, “Anti-frameshifting Ligand Reduces the Conformational Plasticity of the SARS Virus Pseudoknot”, *Journal of the American Chemical Society* 2014 136 (6), 2196-2199. I participated in data analysis. D.B. Ritchie was responsible for data collection and analysis as well as contributed to manuscript edits. W. K.A. Sikkema assisted with the data collection. M.T. Woodside was the supervisory author and was involved with concept formation and manuscript composition. The remaining work in this thesis has not been published in any peer reviewed journals.

Dedication

In memory of my paternal grandfather,

Songliang Soong

1928-2012

and my maternal aunt,

Shiuhui Cheong

1954-2012

Acknowledgements

I would like to express my deepest gratitude towards my supervisor, Dr. Michael Woodside, for being a tremendous mentor. His insight into biophysics opened my eyes and he taught me how a rigorous and careful academic research should be done. I would like to thank my committee members, Dr. Jack Tuszynski and Dr. John Davis, for their invaluable feedback from our previous committee meetings. I would also like to thank Dr. Lindsay Leblanc for her participation in my thesis defense.

I would like to sincerely thank Dr. Armin Hoffman and Dr. Dustin Ritchie for their help and guidance. Dr. Armin Hoffman taught me how to do analysis in a correct and systematic way. Dr. Dustin Ritchie introduced me to many biochemical laboratory techniques.

I would like to appreciate Dr. Hao Yu for his kind explanations on topics that I did not understand. My thesis would not be complete without his effort in collecting the DNA handle and Prion Protein data. I would also like to thank Dr. Krishna Neupane, Dr. Derek Dee, Dr. Allison Solanki and Dr. Daniel Foster for their assistance in various aspects of my research. The rest of the Woodside group have also been helpful.

Finally, I would like to thank my father, mother and brother for their love and support. Furthermore, I would like to dedicate this thesis to my grandfather. May he rest in peace.

Table of Contents

Abstract.....	ii
Preface.....	iii
Dedication.....	iv
Acknowledgements.....	v
Table of Contents.....	vi
List of Tables.....	viii
List of Figures.....	ix
List of Abbreviations.....	xi
1 Conformational Dynamics of Bio-molecules using SM Spectroscopy.....	1
1.1 Introduction.....	1
1.2 Energy Landscape.....	2
1.3 Single Molecule Spectroscopy.....	5
1.3.1 Fluorescence Spectroscopy.....	6
1.3.2 Force Spectroscopy.....	7
1.4 Outline.....	9
2 Force Spectroscopy with Optical Traps.....	10
2.1 Principle of Operation.....	10
2.2 Measurement Modes.....	12
2.2.1 Force-Ramp Measurements.....	13
2.2.2 Force-Clamp Measurements.....	16
2.3 An Approach to Energy Landscape Analysis.....	18
3 Dynamics of the SARS Pseudoknot.....	23
3.1 Ribosomal Frameshifting.....	23

3.2	Single Molecule Experiments.....	27
3.3	Discussion.....	32
4	Mechanical Models for Constant Force Measurements	37
4.1	Motivation	37
4.2	Dynamic Deconvolution of a Network	38
5	Dynamic Deconvolution of Experimental Data	47
5.1	Bead Measurements	47
5.2	Hydrodynamic Effect Measurements.....	52
5.3	Handle Measurements	55
5.4	Protein Measurements	61
6	Conclusion and Future Work.....	68
6.1	RNA pseudoknot conformational dynamics	68
6.2	Dynamic Deconvolution Theory.....	69
	References.....	71

List of Tables

Table 3.1 Summary of results.	31
Table 5.1 Summary of extracted bead radius results.	55

List of Figures

Figure 1.1 Energy landscape.	4
Figure 1.2 spFRET.	6
Figure 1.3 AFM.	7
Figure 1.4 Magnetic tweezers.	8
Figure 2.2 Illustration of optical trapping.	11
Figure 2.2 Schematic of optical tweezers.	12
Figure 2.3 Collection of FECs.	13
Figure 2.4 WLC fits.	14
Figure 2.5 Polymer parameters.	14
Figure 2.6 Sample constant force data.	16
Figure 2.7 Zero stiffness region.	17
Figure 2.8 Key landscape parameters.	20
Figure 3.1 Structure of the SARS CoV pseudoknot.	26
Figure 3.2 Structure of the ligand MTDB.	26
Figure 3.3 FECs of the SARS CoV pseudoknot.	28
Figure 3.4 The distribution of unfolding forces and unfolding rates.	29
Figure 3.5 Mechanical stability and energy landscape parameters.	30
Figure 3.6 Alternate structure formation.	31
Figure 3.7 Percentage of alternatively folded and fraction bound.	32

Figure 4.1 Convoluted system.	39
Figure 4.2 Self and cross response.	40
Figure 4.3 Frequency space response filtering.	44
Figure 4.4 Data analysis procedures.	45
Figure 5.1 Single bead measurements.	48
Figure 5.2 Autocorrelation function of the bead.	49
Figure 5.3 Extracted stiffness comparison.	51
Figure 5.4 Bead response in time and frequency space.	53
Figure 5.5 Summary of bead results.	54
Figure 5.6 Handle measurements.	56
Figure 5.7 Handle response in time and frequency space.	59
Figure 5.8 Handle parameters.	60
Figure 5.9 Bead parameters.	60
Figure 5.10 Protein measurements.	62
Figure 5.11 Unfolded protein response in time and frequency space.	64
Figure 5.12 Folded protein response in time and frequency space.	65
Figure 5.13 Bead parameters with the existence of protein.	66
Figure 5.14 Extracted diffusion coefficient.	66

List of Abbreviations

-1 PRF	Programmed -1 Ribosomal Frameshifting
AOD	Acousto-Optic Deflector
AFM	Atomic Force Microscopy
DNA	Deoxyribonucleic acid
EOD	Electro-Optic Deflector
FDT	Fluctuation Dissipation Theorem
FEC	Force-Extension Curve
MTDB	2-[4-(2-methyl-thiazol-4ylmethyl)-[1,4] diazepane-1-carbonyl]-amino}-benzoic acid ethyl ester
NMR	Nuclear Magnetic Resonance
PrP	Prion Protein
RNA	Ribonucleic acid
SARS	Severe Acute Respiratory Syndrome
SHaPrP	Syrian Hamster PrP
SM	Single-Molecule
spFRET	Single Pair Fluorescence Resonance Energy Transfer
WLC	Worm-Like Chain

1 Conformational Dynamics of Biomolecules using SM Spectroscopy

1.1 Introduction

The conformation of complex macromolecules in cells, such as proteins and nucleic acids, is one of the most studied areas in the field of biochemistry. Nucleic acids (DNA and RNA) and proteins form the basis of an information transfer network which is one of the most important biochemical reaction chains in cells. DNA encodes genetic information that is essential for the assembly and reproduction of every living cell. Proteins perform important functions that are vital to cellular survival, such as catalyzing reactions and serving as building blocks. RNA is involved in protein synthesis and gene regulation (Nelson et al., 2013). Proteins, synthesized by joining amino acid blocks into a single chain, can fold into a highly specific, three dimensional geometric structure through a self-assembly mechanism known as folding. Structural biologists can successfully determine the three dimensional structure of proteins using high-resolution molecular structure tools, including x-ray crystallography and nuclear magnetic resonance (NMR) imaging.

In the early days, a lot of research was focused on the static structure of proteins. For example, the well-known “lock and key” model proposed by Fischer stated that molecular recognition is a result of the complementary conformational geometry between the enzyme and the substrate. The “lock and key” model was an attempt to explain why enzymes are highly specific, but it fails to account for the apparent increase in stability of the enzyme/substrate complex.

Koshland (Koshland, 1995) later suggested a different “induced fit” model, where the enzyme acts as a flexible site that will continue to reshape itself to find the best fit for the conformation of the substrate. Scientists now realize that the conformational dynamics are just as important. Hence, understanding the dynamics of protein structural changes in response to external factors, such as ligand binding and mechanical forces, is important for us to understand the problem of protein folding.

1.2 Energy Landscape

The conformational dynamics of proteins are well described by a framework known as the Energy Landscape Theory (Dill and Chan, 1997). The Energy Landscape Theory was originally developed as a way to understand the problem of how proteins fold (Bryngelson et al., 1995). Anfinsen had previously showed that a protein can spontaneously fold into its native structure after losing its tertiary structure by denaturation (Anfinsen, 1973). Anfinsen conjectured that the protein’s amino acid sequence uniquely determines its tertiary structure, and that the protein’s native structure represents the lowest free energy state. Landscape theory was inspired by the so called Levinthal’s paradox (Levinthal, 1968), a thought experiment estimating the astronomical number of conformations a protein can have. Levinthal showed that it would be impossible for a protein to find its native structure within biologically-meaningful timescales if the folding mechanism involves a random searching process.

As an attempt to resolve Levinthal’s Paradox, Bryngelson and Wolynes incorporated the notion of a molecular Hamiltonian, where energy levels are

assigned to the conformational states of each amino acid residue and their mutual interactions. From a statistical mechanics viewpoint, the folding process favors the equilibrium state of the system that maximizes its microstate multiplicity while minimizing the enthalpy of interactions (Bryngelson and Wolynes, 1987). The energy landscape view of protein folding is, therefore, a geometric visualization of a free energy surface as a function of conformational coordinates. The collection of coordinates describing each residue forms a multi-dimensional phase space, such that the topology of the protein in three dimensional space is completely encoded.

Leopold and colleagues (Leopold et al., 1992) speculated on the geometry of the free energy surface by proposing a funnel-shaped landscape that mandates the protein folding trajectory to eventually reach its native state (Figure 1.1a). The funnel landscape was successful in explaining Anfinsen's experiment: the denatured protein will fold into its native structure regardless of its initial conditions, but with an exponentially quicker timescale compared to a random search, due to the free energy surface gradient. However, a smooth folding funnel fails to account for the existence of metastable intermediate states with energy barriers. Modern theory generally favors a more rugged funnel with bumpy kinetic traps and energy barriers (Figure 1.1b), so that the protein is continuously sampling a wide range of conformation along its rather rough and uneven energy landscape until it reaches an equilibrium. At the finest level, the energy landscape is riddled with many local minima (Bryngelson et al., 1995). These local minima are usually connected to local changes at the atomic level, such as the rotation of side chains.

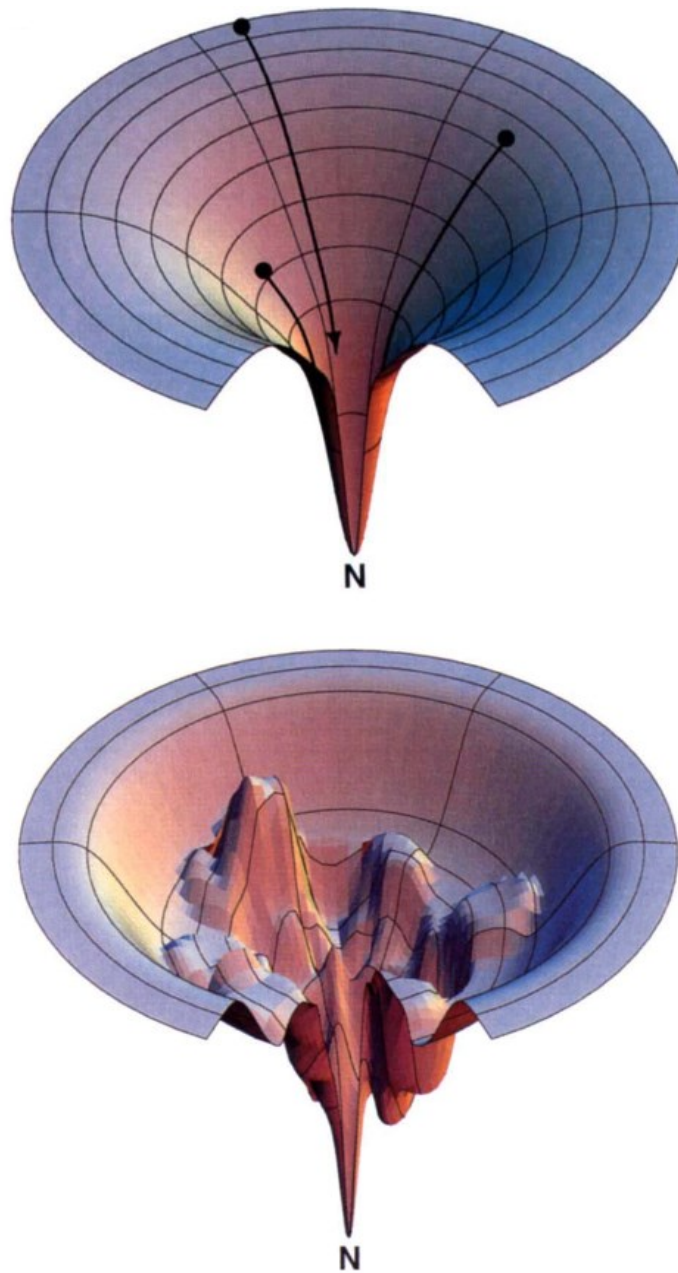


Figure 1.1: A three dimensional projection of the hypothetical free energy surfaces. Vertical axis shows the free energy value as a function of two conformational coordinates such as dihedral angle. (Top) A smooth funnel. (Bottom) A rugged energy landscape with bumpy kinetic traps and energy barriers. Figure adapted from (Dill and Chan, 1997)

Several works (Bryngelson and Wolynes, 1989; Zwanzig, 1988) have modeled protein folding as a diffusive search for the native structure over a rough energy landscape. The surface roughness directly affects the lifetimes and rates of the transition states, and consequently changes the apparent coefficient for conformational diffusion over the landscape. We are interested in extracting information that characterizes the energy landscape, such as the barrier properties and the conformational diffusion coefficient, from single molecule measurements, in order to fully understand the conformational dynamics of proteins.

1.3 Single Molecule Spectroscopy

Single molecule (SM) experiments provide invaluable insight into the dynamics of molecules by measuring the properties of individual molecules instead of ensembles of many molecules. Ensemble measurements can only provide the average behavior of the molecule, therefore the details of the stochastic fluctuations are lost. On the other hand, SM spectroscopy can be used to observe rare or transient events and can distinguish different populations of behavior, allowing for example on or off pathway intermediates that would normally be lost in ensemble measurements to be characterized (Weiss, 1999). Due to the ability to probe extremely fast dynamics, typically down to the sub-millisecond regime, SM spectroscopy allows us to monitor the real time motion of molecules instead of their time-averaged movements.

The literature of SM experiments is mainly divided according to the methods used to probe individual molecules, most commonly fluorescence and

force spectroscopy. Each method has advantages and disadvantages. For example, force spectroscopy allows one to manipulate the system under non-equilibrium conditions, but requires the molecule to be connected to a large force probe. No such invasive probe is involved in fluorescence spectroscopy, allowing more subtle internal dynamics of the molecule to be probed, but it is harder to manipulate the conformation of the molecule actively as in force spectroscopy.

1.3.1 Fluorescence Spectroscopy

One of the most widely used fluorescence techniques is the Single Pair Förster Resonance Energy Transfer (spFRET). This technique involves the distance dependent transfer of energy from a donor fluorophore to an acceptor fluorophore. The excited donor transfers its energy non-radiatively to a nearby acceptor fluorophore. The spFRET technique is a sensitive tool used to probe conformational changes in a characteristic distance scale, known as the Förster radius (Ha *et al.*, 1996) and has been used to study conformational changes occurring during processes such as ligand binding to a receptor, enzyme-substrate catalysis, and diffusive motion (Weiss, 1999).

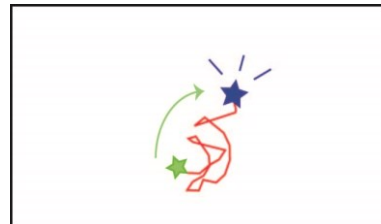


Figure 1.2: spFRET. Molecules are labeled by a pair of donor-acceptor fluorophores. The FRET efficiency is directly related to the inversed sixth-squared power of the distance between them.

1.3.2 Force Spectroscopy

Force spectroscopy, the technique used in this thesis, probes the molecule by applying force and measuring the change in length as the protein structure unfolds and refolds. For example, a common approach in force spectroscopy is to study the relationship between the force applied to the molecule and the extension of the polymer chain, known as the force-extension curve (FEC) (Neuman and Nagy, 2008). Conformational dynamics information such as the lifetime and transition rates of states can be extracted from the FECs and used to reconstruct the energy landscape.

Atomic Force Microscopy (AFM) is the most widely used single molecule instrument, with numerous applications in a variety of disciplines. In biophysical studies of protein folding, AFMs are used to apply force to a single molecule, by tethering it at one end to a surface and the other end to the tip of a cantilever, and then pulling the cantilever up vertically. The force on the molecule deflects the tip of the cantilever, and when the molecule experiences an unfolding or bond breaking event, there is a sudden change in the cantilever position.

Therefore, AFMs are used to probe structural changes in biomolecular systems as diverse as polysaccharides (Rief et al., 1997), muscle protein titin (Rief et al., 1998), and biotin-avidin interactions (Lee et al., 1994).

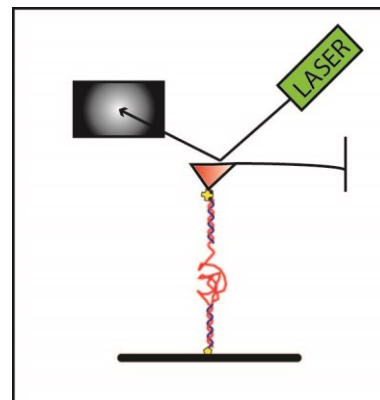


Figure 1.3: AFM. Molecules are anchored to a flat surface on one end and connected to the tip of a cantilever on the other end. The cantilever position will be deflected when a folding/unfolding event occurs.

Another way to apply force to molecules uses magnetic tweezers. Magnetic tweezers employ magnetic fields as means to manipulate paramagnetic particles attached to the molecule of interest. The particle can also be subjected to a torque, so that experiments can be designed relatively easily to accommodate rotational measurements (Greenleaf et al., 2007). Magnetic tweezers serve as a great tool to study structural changes, such as the behavior of DNA under twisting conditions (Mosconi et al., 2009; Zlatanova and Leuba, 2003) and dissociation of ligand-receptor complexes (Danilowicz et al., 2005).

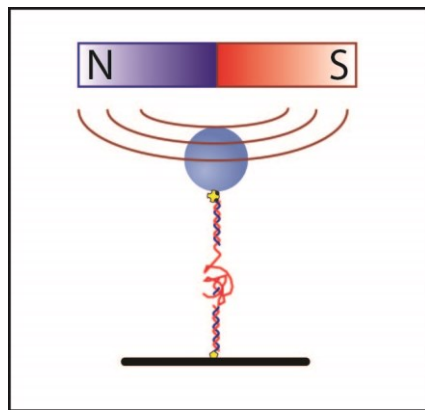


Figure 1.4: Magnetic tweezers. Molecules are tethered between a paramagnetic bead and a surface. The bead will experience force and torque when a magnetic field is applied.

A third method commonly used to apply force to molecules is optical trapping. Optical trapping is based on the principle that light exerts force on a dielectric particle, such as a polystyrene bead. This bead is then typically connected to the molecule of interest via a DNA handle, to allow the molecule to be manipulated. Optical tweezers can measure molecular movements with sub-nanometer accuracy and sub-millisecond time resolution (Neuman and Nagy, 2008). They have been employed to study conformational dynamics of

biomolecules, such as prion protein (Yu et al., 2012, 2013), RNA pseudoknots (Ritchie et al., 2012), and adenine riboswitch (Frieda and Block, 2012). This thesis focuses on using optical tweezers as a tool to probe conformational dynamics of biomolecules.

1.4 Outline

The main focus of this thesis is to investigate how dynamical information can be found from a single molecule using optical tweezers. Chapter 2 discusses the experimental setup of optical tweezers, the various types of measurement modes available, and how to analyze data. Chapter 3 applies the data analysis methods to the RNA pseudoknot from the Severe Acute Respiratory Syndrome (SARS) coronavirus, demonstrating how the pseudoknot conformational dynamics affect programmed frameshifting, a mechanism that is vital for the virus life cycle. Chapter 4 discusses how to understand the mechanics of each component in an optical trapping measurement in more detail by using the Dynamical Deconvolution Theory developed by Hinczewski and colleagues (Hinczewski et al., 2010). Chapter 5 discusses the application of Hinczewski's theory to constant force measurements of beads, handle and prion protein. Finally, chapter 6 provides a summary and discusses possible future work.

2 Force Spectroscopy with Optical Traps

2.1 Principle of Operation

In 1970, Ashkin showed that by using focused laser beams, the dynamics of a transparent, micron-sized particle in fluid can be affected significantly from the scattering and gradient force of the light (Ashkin, 1970). Optical trapping in fluids, as required for studies of biological molecules, was first demonstrated in 1986 (Ashkin et al., 1986). With rapid advancement over the following years, optical traps are now used to study many questions in biophysics, probing the mechanical and elastic properties of bio-molecules via pulling experiments (Ashkin, 2000).

Optical trapping relies on the principle that a photon exerts momentum when it scatters from a dielectric object. A photon carrying momentum $p = h/\lambda$, where h is the Planck's constant and λ is the wavelength of the light, transfers its momentum and exerts a net force when it scatters off of a particle. The net force exerted by light can be decomposed into two components: the scattering and the gradient force. The scattering force, which is in the direction of light propagation, comes from the absorption and re-radiation of photons. The scattering force strength depends on the refraction index of medium (n_m), laser intensity (I), the scattering cross section (C), and the speed of light in a vacuum (c).

$$F_{scat} = \frac{n_m C I}{c} \quad [2.1]$$

The scattering force does not give rise to stable trapping. Instead, trapping is due to the gradient force, which arises from the gradient in the electromagnetic field

strength within the tightly-focused laser beam. The energy of the polarizable dielectric particle in the laser beam is lowest at the most intense part of the beam the focal point, hence the gradient in the light intensity produces a force directed to the focal point (Figure 2.1) (Harada and Asakura, 1996). The scattering force will act to push the particle away from the focal point, but if it is sufficiently small, it can be overcome by the gradient force, producing a stable trap close to the focal point, at the location where the two forces are in balance. For small displacements from the center of the trap, the optical trap behaves like a Hookean spring: the trapped object will experience a linear restoring force, $F = -kr$, where r is the displacement from the trap center, and k is the trap stiffness, typically ranging from 0.1 to 1 pN/nm.

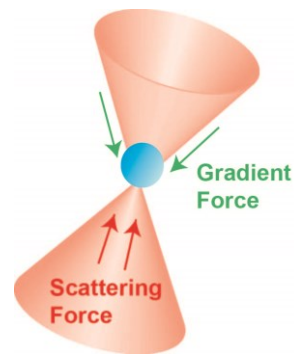


Figure 2.1: Illustration of an optical trapping. The force acting on a trapped bead can be decomposed into two components: the scattering force (red arrow) and the gradient force (green arrow). Stable trapping will occur when the two forces are in balance.

Our laboratory employs a 1064-nm Nd:YVO₄ diode-pumped solid state laser as the trapping laser. The laser beam is split into two beams with orthogonal polarization to create two traps. The position of each trap is controlled in two axes using acousto-optic deflectors (AODs) and/or electro-optic deflectors (EODs), depending on the instrument, which allow the beam deflection to be controlled precisely. In addition to trapping lasers, our dual-trap optical tweezers system utilizes a second laser at a different wavelength (633 nm or 830 nm, depending on the instrument), again split into two beams with orthogonal

polarization (one for each trap), to probe the bead in each of the two traps. The light from the detection beams is scattered by the trapped beads; this light is captured by position sensitive detectors (PSD), which are used to determine the position of the beads in the traps.

Optical tweezers do not apply force directly to the molecule of interest. Experiments are usually done by first preparing constructs in which the molecule of interest is attached to long double stranded DNA handles, then attaching each handle to a micron-sized dielectric bead (Figure 2.2). The handles are needed because the two optical traps have to be separated by approximately one wavelength apart to avoid significant interference and cross talk. Force can be applied to the construct by moving the traps apart and causing a bead to move out of the trap center, thus exerting a restoring force on the bead.

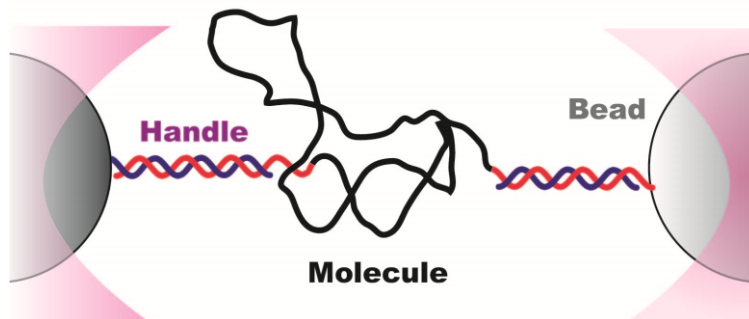


Figure 2.2: Schematic of optical trapping measurement. The molecule is connected to a pair of polystyrene beads via DNA handles. Note that the figure is not drawn to scale.

2.2 Measurement Modes

Measurements using optical tweezers can be divided into two broad categories: the force-ramp and the force-clamp. In force-ramp measurements, the force is

ramped up and/or down by moving the traps apart, usually at a constant speed. Often the force is changed rapidly compared to the folding and unfolding rate for the molecule, such that the molecule is not in equilibrium during the measurement. In force-clamp measurements, on the other hand, the molecule is held at a constant force, for example by using a feedback loop (Liphardt et al., 2001). As a result, the molecule is probed under equilibrium conditions. In both of these cases, the observable being measured is the position of the two trapped beads. Knowing the location of each trap, the radius of the beads, and the stiffness of each trap, we can calculate the end-to-end extension of the construct being measured (handles plus molecule of interest) as well as the force being applied to it.

2.2.1 Force-Ramp Measurements

Force-ramp measurements are made by pulling on the bead-handle-molecule construct with a force that changes with time, for example ramping the force up to unfold the molecule then bringing it back down to allow the molecule to refold. This will result in a set of force-extension curves (FECs), obtained by repeatedly pulling and relaxing the molecule (Figure 2.3). The force is usually changed by moving the traps apart with a constant velocity.

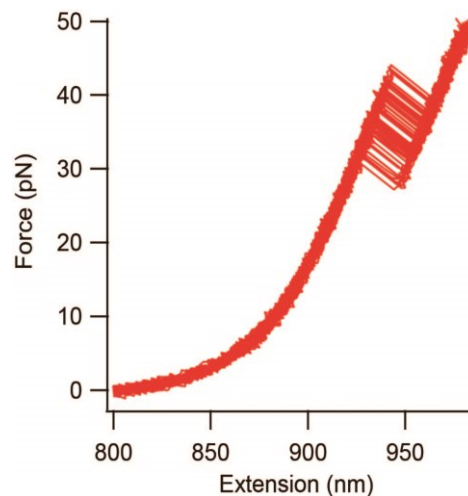


Figure 2.3: A collection of FEC curves showing unfolding of a RNA molecule. The molecule unfolds at different force each time due to the stochastic nature of the unfolding process.

As the molecule is being pulled, mechanical unfolding can be observed as a sudden increase in the molecular extension, with a simultaneous decrease in the force (Figure 2.4, black line). The extension increases because the polymer chain of the unfolded molecule is stretched out under tension, while the force decreases because the increase in the length of the molecule allows the beads to move back towards the center of the traps.

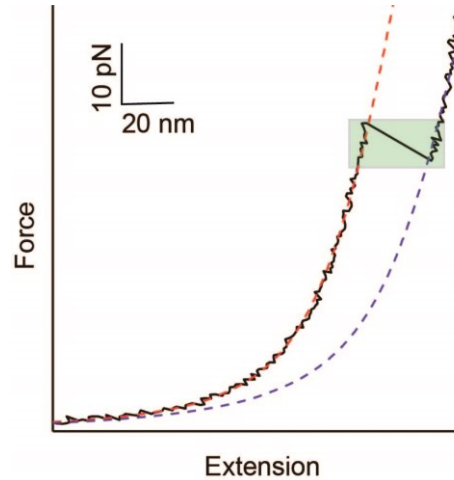


Figure 2.4: WLC fits to the folded (red dashed line) and the unfolded (blue dashed line) part of the FEC. The green region shows the range where constant force measurements are made.

From FECs like the one in Fig 2.4, the change in extension can be used to determine the length of the polymer chain forming the structure that was unfolded, by fitting the

FECs to a model of polymer elasticity such as the extensible worm-like chain (WLC) model. The WLC model treats the molecule as an elastic rod that can bend (Figure 2.5). The relationship between force and

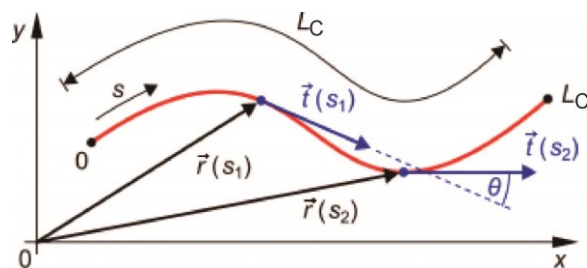


Figure 2.5: Worm-like chain polymer model. L_c is defined as the length of the backbone of the polymer chain, while L_p is the length over which correlations between tangent vectors decay exponentially. Figure adapted from (diploma thesis of Steve Pawlizak, University of Leipzig, 2009).

extension expected for the WLC model is given by Equation 2.2 (Marko and Siggia, 1995):

$$F(x) = \frac{1}{\beta L_p} \left[\frac{1}{4} \left(1 - \frac{x}{L_c} + \frac{F}{K} \right)^{-2} - \frac{1}{4} + \frac{x}{L_c} - \frac{F}{K} \right] \quad [2.2]$$

Here L_c denotes the contour length of the polymer (the length along the backbone of the polymer chain), L_p denotes the persistence length (the length over which correlations in the tangent vector decay), and K denotes the enthalpic elasticity of the molecule (reflecting the bending of molecular bonds under tension). $\beta = 1/k_B T$ is the inverse thermal energy, where k_B is the Boltzmann's constant and T is the temperature.

To determine the change in the contour length of the molecule upon unfolding, we first fit the part of the FEC before the “rip” where unfolding occurs to Equation 2.2 (Figure 2.4, red dashed line). Equation 2.2 is seen to describe the data very well. This part of the curve, where the molecule is folded, involves the extension of the DNA handles only. We next fit the part of the FEC after the unfolding “rip”, where the extension includes both the handles and the unfolded molecule (Figure 2.4, blue dashed line). Here we model it as two WLCs in series, one for the DNA handles and one for the molecule being unfolded. We use the same parameters for the DNA handle WLC as from the fit before the molecule unfolds. We also simplify the fitting by using literature values for L_p and K of the molecule being unfolded, so that the only remaining free parameter is the contour length change of the molecule during the unfolding transition ΔL_c . The contour length change of the molecule indicates how many nucleotides (for nucleic acids) or amino acids (for proteins) unfolded, hence providing us with information about the structure involved in the unfolding process.

Apart from contour length changes, there are a lot of interesting properties of the conformational dynamics than can be extracted from force-ramp measurements. For example, rates can be derived from the unfolding force distributions, and they can be analyzed to characterize the energy landscape for the molecule (as described below in section 2.3). One limitation of force-ramp experiments is that energy is dissipated because the measurements are out of equilibrium, making it harder to extract equilibrium information. However, fluctuation theorems can be used to recover the equilibrium properties. For example, the total free energy change can be found by using either the Jarzynski equality or Crook's Theorem (Crooks, 1999; Jarzynski, 1997). Hummer and Szabo also showed that the profile of the free energy landscape can be reconstructed from non-equilibrium pulling experiments (Hummer and Szabo, 2001).

2.2.2 Force-Clamp Measurements

In force-clamp measurements, the molecule is held under equilibrium conditions by maintaining a constant applied force. These experiments are essentially exploiting the region of the FECs around the unfolding force where the molecule can exist in different

extensions at a given force

(Figure 2.4, green area). In

this range of forces, the

molecule can hop between

different states, changing

extension as it unfolds or

refolds (Figure 2.6). The

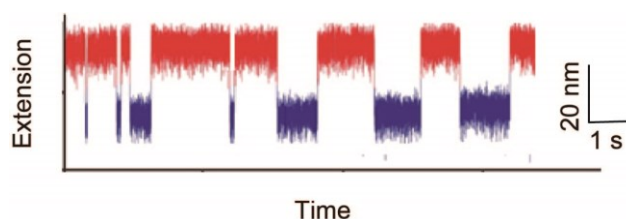


Figure 2.6: A sample data trace from constant force measurements, showing fluctuations in the extension as a function of time. Different states are identified by the extension along the pulling axis: red is the unfolded state and blue is the folded state. The extension also fluctuates rapidly within each state.

corresponding contour length change can be calculated using the extensible WLC model (Equation 2.2). In addition to monitoring transitions between states, for example folded (blue) and unfolded (red) in Figure 2.6, force-clamp measurements can also measure the fluctuation of the extension within each state. As we will see in Chapter 4, these fluctuations can be analyzed to determine the coefficient for conformational diffusion in each state.

Force-clamp experiments can be further subdivided into two categories depending on how the constant force is maintained: the active clamp, in which constant force is maintained by employing a feedback mechanism, and the passive clamp, which makes use of the anharmonic part of the trapping potential to maintain a constant force (Greenleaf et al., 2005). To understand the passive clamp, note that as the bead is moved away from the trap center, eventually the Hookean spring approximation is no longer valid. The gradient force becomes non-linear, causing the force-displacement curve to roll over and creating a 30-50 nm region where the force remains

approximately constant (to within a few percent). If one pulls the bead onto the maximum of the force-displacement curve, where the trap stiffness is effectively zero (Figure 2.7, red area), then motion of the bead as the molecule unfolds and refolds doesn't lead to any change in force, thereby achieving a constant force. The desired force

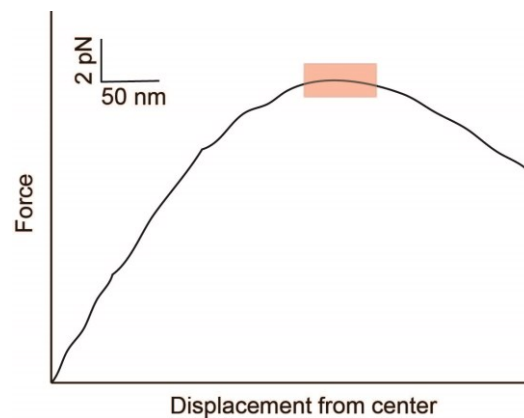


Figure 2.7: The bead is pulled out of the center of the trap to the zero-stiffness region (red box), where the force is approximately constant over a window roughly 50nm wide.

can be applied simply by increasing the laser intensity on the other end, such that it is still in the linear region of the force-displacement curve. This technique can lead to a significant increase in bandwidth as it is relaxed from the stricter position range of traditional feedback loops. In constant trap separation measurements, the instantaneous force of the system changes according to end-to-end extension fluctuations.

Force-clamp experiments are especially useful to detect very rare or short-lived states because each state is represented by a unique extension and they can be observed for a long time (Neupane et al., 2011; Yu et al., 2012). Several methods based on correlation analysis have been developed in order to extract the conformational dynamics of a molecule under constant force experiments (Hinczewski et al., 2010; Hoffmann and Woodside, 2011). Further details will be addressed in Chapter 4.

2.3 An Approach to Energy Landscape Analysis

As motivated in chapter 1, understanding the dynamics of a molecule and how it responds to changes in external factors such as force will provide us with a more complete picture of the mechanics of folding. As it happens, both types of force spectroscopy measurements allow us to extract the same kind of information, just under different conditions. This equivalency was confirmed by Dudko and colleagues, when they showed how the results from force-ramp measurements can be mapped onto the results from constant force measurements via the force-dependent rate (Dudko et al., 2008).

As discussed in section 1.2, the energy landscape can in principle be reconstructed if we know the energy of the molecule as a function of all possible orientations of the bond angles in the peptide chain. However, this is unrealistic due to experimental and computational limitations. As an alternative, we can project the hyper-dimensional free energy surface onto a single axis, known as the reaction coordinate, which we use to follow the progress of the folding reaction. The reaction coordinate is usually chosen to be the experimental observable; in the case of force spectroscopy measurements, this is the extension along the pulling axis (Gupta et al., 2011). It is important to keep in mind that there are still controversies on whether the projection along the pulling axis fully captures the energy landscape (Dudko et al., 2011).

In any given force-ramp measurement, the molecule unfolds at a particular value of applied force, but this value can be different each time the molecule is pulled because the unfolding is driven by thermal fluctuations (Figure 2.3). Repeated force-extension curves therefore give a probability distribution for the unfolding force, $p(F)$.

$$p(F) = \frac{k(F)}{r} \exp\left[-\frac{k_0}{\Delta x^\ddagger r} - \frac{k(F)}{\Delta x^\ddagger r} \left(1 - \frac{vF\Delta x^\ddagger}{\Delta G^\ddagger}\right)^{1-1/\nu}\right] \quad [2.3]$$

Here $k(F)$ is the force-dependent unfolding rate, k_0 is the unfolding rate at zero force, Δx^\ddagger is the distance from the folded state to the energy barrier (or transition state) for unfolding, ΔG^\ddagger is the height of the energy barrier from the folded state, r is the force loading rate, and ν is a scaling factor related to the functional form of the underlying free energy profile ($\nu = 2/3$ for a linear-cubic potential as shown in Figure 2.8, $\nu = 1/2$ for a cusp-shaped barrier). This distribution depends on

various factors, such as the force loading rate (rate of change of force) and the unfolding rate of the molecule (Dudko et al., 2008). It can be modeled as a function of the key parameters of the energy landscape (Figure 2.8) (Dudko et al., 2006):

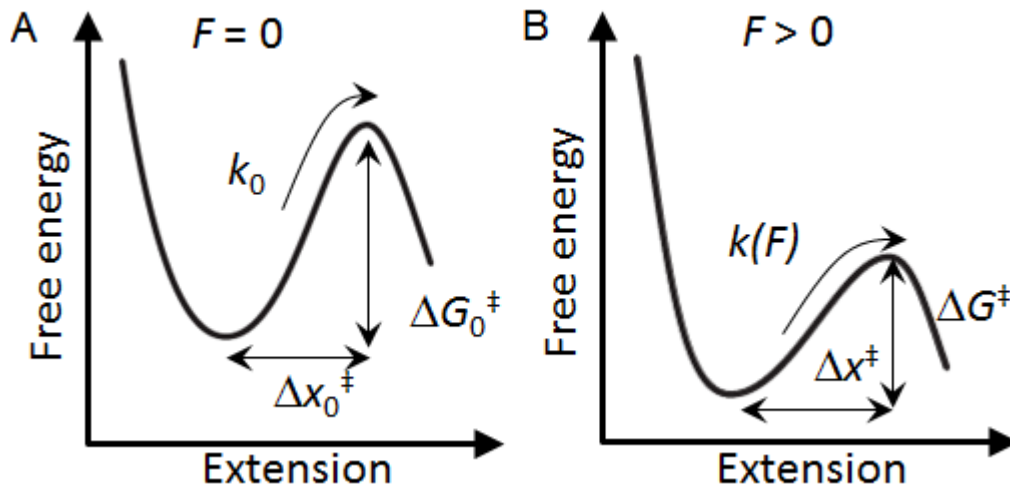


Figure 2.8: A typical one dimensional projection of the energy landscape (a) in the absence and (b) in the presence of force. The key parameters characterizing the landscape is the barrier height (ΔG^\ddagger), the distance to barrier (Δx^\ddagger) and the rate of escape from the folded state (k). Figure adapted from (Dudko et al., 2006).

A simple functional form of the force-dependent unfolding rate, $k(F)$, was proposed by Evans and Ritchie (Equation 2.4) (Evans and Ritchie, 1997), based on earlier work by Bell (Bell, 1978) estimating reaction rates for membrane bound reactants. It is a purely phenomenological equation that describes some data fairly well:

$$k(F) = k_0 e^{-\beta F \Delta x^\ddagger} \quad [2.4]$$

The Bell-Evans equation was derived based on the assumption that force only changes the barrier height, which is known to be inaccurate because the barrier position changes according to force as well (Dudko et al., 2006). To address these limitations, Dudko and colleagues proposed a modified functional form for $k(F)$ (Equation 2.5). Equation 2.5 was derived based on the generalization of Bell's formula in Kramers' theory (Dudko et al., 2008), under the assumption of specific functional forms for the profile of the energy landscape.

$$k(F) = k_0 \left(1 - \frac{\nu F \Delta x^\ddagger}{\Delta G^\ddagger}\right)^{1-1/\nu} e^{-\beta \Delta G^\ddagger [1 - (1 - \nu F \Delta x^\ddagger / \Delta G^\ddagger)^{1/\nu}]} \quad [2.5]$$

Here ν parameterizes the landscape profile as in Equation 2.3 (Dudko et al., 2006). In the case of $\nu = 1$, Equation 2.5 reduces to Bell's equation (Equation 2.4). Using Equations 2.3 and 2.5, we can readily extract the energy landscape parameters from fitting the unfolding force histogram obtained from force-ramp measurements. Since the precise shape of the barrier is often unknown, we can average the landscape parameters extracted from both cases ($\nu = 2/3$ and $\nu = 1/2$).

A caveat to keep in mind, however, is that while k_0 is the reaction rate at zero force, measurements can never be done in the absence of force. It is therefore necessary to extrapolate the non-zero rates to obtain the reaction lifetimes. However, due to the exponential relationship between the stretching force and the lifetimes, the error of estimation can be significant. Careful error analysis is required before k_0 can be interpreted as the effective reaction rate at zero force.

Dudko *et al.* also demonstrated a mapping between force-clamp and force-ramp experiments (Dudko et al., 2008). The expected lifetime of a molecule

in a particular state at a given force, $\tau(F)$, as measured in force-ramp experiments, can be calculated by using equation 2.6. Here $\dot{F}(F)$ denotes the force loading rate.

$$\tau(F) = \int_F^{\infty} p(f)df / [\dot{F}(F)p(F)] \quad [2.6]$$

This relation essentially provides a framework for transforming the rupture force distribution into lifetimes (or rates, which are the inverse of the lifetimes) at a constant force.

3 Dynamics of the SARS Pseudoknot

RNA plays a vital role in facilitating a wide variety of cell functions. While DNA is primarily involved in the encoding of genetic information, RNA plays many different roles, including the regulation of protein synthesis, catalyzing biochemical reactions, and sensing cellular signals, to name a few. Due to its single stranded nature, RNA can fold into more versatile structures than can double stranded DNA. For example, one interesting structure that is found in RNA is the pseudoknot, a conformation of RNA in which the loop of a hairpin structure is base-paired to another part of the RNA strand. This chapter will apply the data analysis techniques discussed in chapter 2 to investigate the conformational dynamics of pseudoknots as revealed by force extension curves. The biological importance of this study and its relevance to the field of drug design will also be discussed.¹

3.1 Ribosomal Frameshifting

Ribosomes synthesize proteins by reading messenger RNA (mRNA) in 3-nucleotide (nt) steps, maintaining a specific reading frame until a stop codon is reached. In programmed -1 ribosomal frameshifting (-1 PRF), the ribosome skips backward on the mRNA by 1 nt, typically resulting in the bypass of a stop codon and the translation of a new reading frame specifying a different amino acid sequence (Brierley et al., 2010; Giedroc and Cornish, 2009). Many RNA

This chapter has been published as Dustin B. Ritchie, Jingchuan Soong, William K. A. Sikkema, and Michael T. Woodside, "Anti-frameshifting Ligand Reduces the Conformational Plasticity of the SARS Virus Pseudoknot", *Journal of the American Chemical Society* 2014 136 (6), 2196-2199.

viruses make use of -1 PRF to produce structural and enzymatic proteins in tightly regulated ratios (Dinman and Wickner, 1992; Dulude et al., 2006; Telenti et al., 2002). For example, the Severe Acute Respiratory Syndrome coronavirus (SARS CoV) uses -1 PRF to regulate production of RNA-dependant RNA polymerase and other replicase proteins (Thiel et al., 2003). Altering the -1 PRF efficiency can greatly reduce SARS virus infectivity (Plant et al., 2010, 2013); a similar effect has also been demonstrated for HIV (Dulude et al., 2006; Shehu-Xhilaga et al., 2001; Telenti et al., 2002). The importance of -1 PRF efficiency to virus replication has motivated efforts to develop new anti-viral therapeutics that target the frameshifting mechanism in viruses such as HIV (Brakier-Gingras et al., 2012) and SARS (Ahn et al., 2011; Park et al., 2011).

Frameshifting depends on two specific components in the mRNA: a 7-nt “slippery sequence” at which -1 PRF occurs, and a stimulatory structure, usually a pseudoknot, located 6–8 nt downstream (Brierley et al., 2010; Giedroc and Cornish, 2009). Efforts to reduce viral infectivity by modulating frameshifting efficiency have primarily focused on identifying small molecules that bind to the stimulatory structures or developing anti-sense oligonucleotides to alter them. Small molecules that modulate frameshifting efficiencies for SARS CoV (Ahn et al., 2011; Park et al., 2011) and HIV-1 (Brakier-Gingras et al., 2012) have indeed been found, but interpreting the effects of such molecules can be complicated. The mechanism of binding is not always known, nor are the effects of binding on the stability and structure of the stimulatory RNA, and the interactions with the stimulatory RNA may not be specific. Most importantly, the mechanisms by which the compounds regulate -1 PRF are unclear. For example, some compounds with promise against HIV-1 likely bind RNA in general, rather than

specific stimulatory structures, suggesting that they may modulate frameshifting efficiency via interactions with ribosomal RNA (the RNA contained within the ribosome itself) (Brakier-Gingras et al., 2012; Marcheschi et al., 2011).

A complicating factor in efforts to develop drugs that target frameshifting is the fact that the mechanism of -1 PRF is still incompletely understood, especially the role of the stimulatory structure in determining -1 PRF efficiency. Models have been proposed with -1 PRF occurring at various steps in the elongation cycle (Brierley et al., 2010; Giedroc and Cornish, 2009; Jacks et al., 1988; Namy et al., 2006; Plant and Dinman, 2005; Plant et al., 2003). The tension generated in the mRNA as the ribosome unwinds the stimulatory structure plays a key role in several of these models. For example, one commonly-cited model posits that the pseudoknot acts as a mechanical roadblock to ribosome translocation, weakening the codon-anticodon base pairing when the ribosome is over the slippery sequence and thereby promoting a -1 shift in reading frame (Kontos et al., 2001; Namy et al., 2006). Direct measurements of translocating ribosomes do show that tension in the tRNA-mRNA linkage is used by the ribosome to promote unwinding of structured RNAs at the mRNA entry site (Qu et al., 2011).

However, -1 PRF efficiency is not determined by the thermodynamic stability of pseudoknots (Chen et al., 1995; Kang et al., 1996; Napthine et al., 1999), nor is it correlated with pseudoknot-induced ribosomal pausing (Kontos et al., 2001) as would be expected from this picture. Early studies using mechanical tension to mimic how the ribosome unwinds RNA structure suggested a correlation with resistance to mechanical unfolding (Chen et al., 2009; Hansen et al., 2007), but recently a more comprehensive survey of pseudoknot unfolding

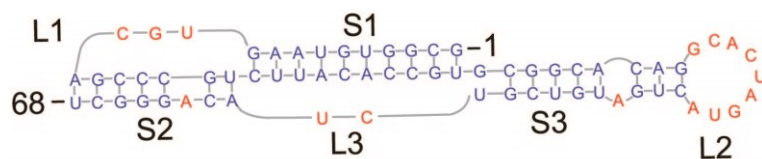


Figure 3.1: The SARS CoV pseudoknot consists of 3 stems (S1–S3) and 3 loops (L1–L3), indicated on the secondary structure. Base-pairs are shown in blue, unpaired nucleotides in red.

showed that -1 PRF efficiency was not, in fact, determined by any characteristic of the mechanical unfolding (Ritchie et al., 2012). Instead, -1 PRF efficiency was unexpectedly found to correlate with the conformational plasticity of the pseudoknot, as reflected in its ability to form alternate structures.

To confirm the notion that pseudoknot conformational dynamics is a factor determining -1 PRF efficiency and test whether it provides a useful basis for designing anti-frameshifting drugs, we focused on the binding of an anti-frameshifting ligand to the SARS CoV pseudoknot. The SARS CoV pseudoknot has an unusual three-stemmed structure (Figure 3.1) (Baranov et al., 2005; Plant et al., 2005; Su et al., 2005), in contrast to the two-stemmed hairpin-type pseudoknots more commonly employed by viruses to stimulate -1 PRF (Giedroc and Cornish, 2009).

Recently, *in silico* screening for compounds that bind the SARS CoV pseudoknot, based on calculations of the energy of the ligands docked against the pseudoknot, found a small molecule referred to as MTDB (Figure 3.2), that

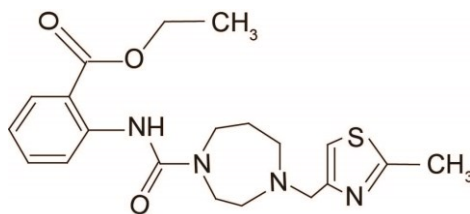


Figure 3.2: Structure of the ligand, 2-{{4-(2-methyl-thiazol-4ylmethyl)-[1,4] diazepane-1-carbonyl}-amino}-benzoic acid ethyl ester (MTDB).

suppresses -1 PRF in both cell-free and cellular translation systems (Park et al., 2011). The effect was specific to the SARS pseudoknot, as no reduction in -1 PRF was observed for two other pseudoknots tested as negative controls.

3.2 Single Molecule Experiments

The effect of MTDB binding on the mechanical stability and structural dynamics of the SARS CoV pseudoknot was tested using optical tweezers. The RNA was held near zero force for 3 s in 50 mM MOPS, pH 7.0, 130 mM KCl, 4 mM MgCl₂, 0.3% DMSO to permit folding and ligand binding, then the traps were separated at constant velocity to apply force while measuring molecular extension, thereby generating force-extension curves (FECs) as described in Chapter 2 (Figure 3.3). With or without ligand present, unfolding occurred most commonly as a two-state process without intermediates (Figure 3.3, black). The change in contour length during such unfolding events, ΔL_c , was found by fitting the folded and unfolded branches of the FECs (Figure 3.3, red and purple, respectively).

The result, $\Delta L_c = 33 \pm 1$ nm (all errors represent standard error on the mean), agrees well with the value 34 nm expected from the predicted secondary structure,(Plant et al., 2005; Su et al., 2005) assuming an end-to-end distance in the folded structure of 6 nm similar to the infectious bronchitis virus pseudoknot (Green et al., 2008) and consistent with the tertiary structure proposed from computational work (Park et al., 2011). The pseudoknot was thus natively folded in these curves. However, without ligand present, a substantial minority (30 ± 3 %) of the curves displayed unfolding at a lower force and with an unexpectedly short ΔL_c , 21 ± 1 nm, indicating that the pseudoknot was folded into

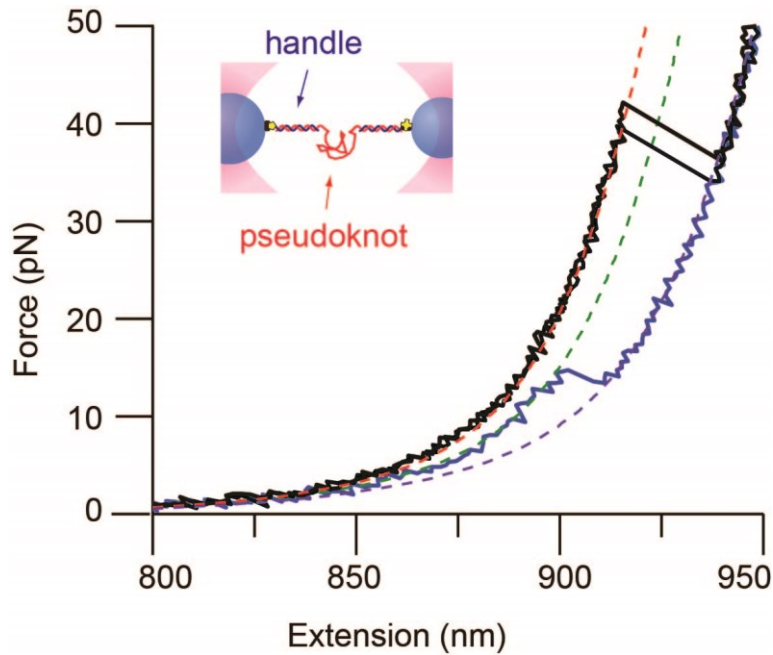


Figure 3.3: A single SARS CoV pseudoknot molecule was tethered between two beads held in optical traps (inset). The RNA contour length changes abruptly upon unfolding, causing a “rip” in the FEC. Most FECs showed a length change, found from WLC fits to Equation 2.2 (dashed lines), consistent with the native structure (black), but some (blue) revealed a smaller, alternate structure.

an alternate structure at the start of those pulls (Figure 3.3, blue; WLC fit: green). The distributions of ΔL_c and unfolding force suggest only a single alternate conformation is present. Increasing the waiting time between pulls to 10 s did not change the extent of alternate structure formation noticeably, suggesting that any inter-conversion between the structures is very slow.

We can quantify the resistance of the pseudoknot to mechanical unfolding from the distribution of unfolding forces, $p(F)$. The average unfolding force for the native structure without ligand bound was 42 ± 1 pN. Additionally, the height of the energy barrier for unfolding, ΔG^\ddagger , the distance to the barrier from the folded state, Δx^\ddagger , and the unfolding rate at zero force, k_o , were found by fitting $p(F)$

to the kinetic theory as mentioned in chapter 2 in Figure 3.4a (Equation 2.3). The unfolding rate as a function of force, was also well fit by Equation 2.5 (Figure 3.4b). Data were analyzed by both methods and the results averaged, yielding $\log k_0 = -4.4 \pm 0.3 \text{ s}^{-1}$, $\Delta x^\ddagger = 1.6 \pm 0.1 \text{ nm}$, and $\Delta G^\ddagger = 41 \pm 3 \text{ kJ/mol}$ for the pseudoknot without ligand.

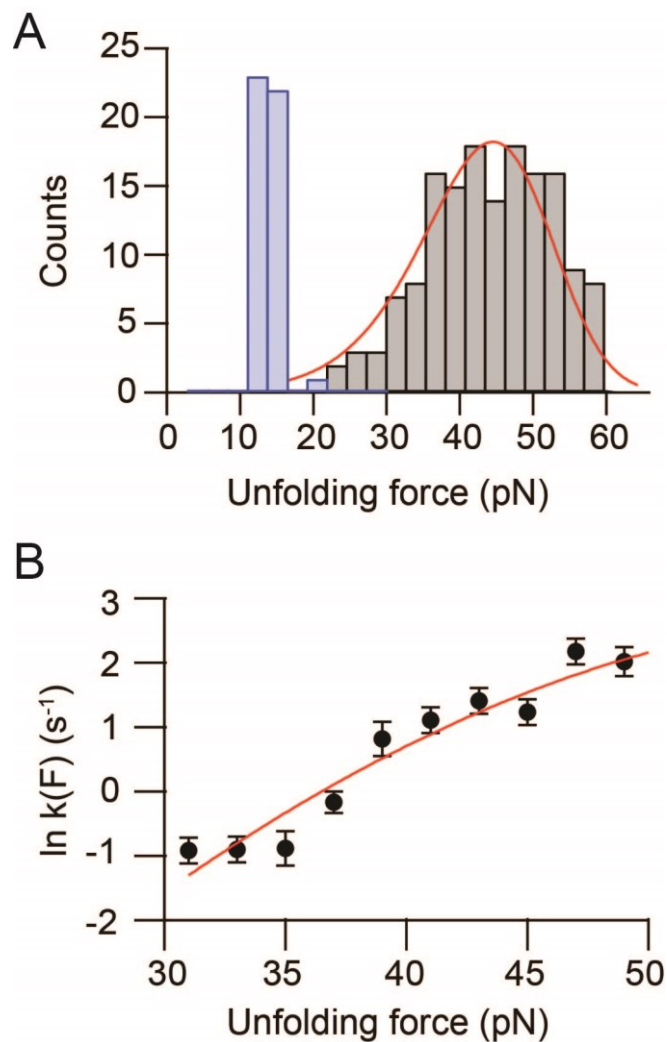


Figure 3.4: (a) The distribution of unfolding forces for the native pseudoknot in the absence of ligand (black) was fit to Equation 2.3 to determine the energy landscape parameters for mechanical unfolding. The alternate structure unfolded at a significantly lower force (blue). (b) The force-dependent unfolding rate was fit to Equation 2.5.

We repeated these measurements with three concentrations of MTDB: 75, 250, and 500 μM . Qualitatively, the behavior of the pseudoknot was similar in all cases; there were no additional sub-populations in the pulling curves, such as curves in which the RNA did not unfold (a possible result of covalent cross-linking by the ligand) or refold (a possible result of binding to the unfolded RNA). The average unfolding force and landscape parameters for the native structure were found to remain the same, within error; any changes were too subtle to detect (Figure 3.5, Table 3.1). Hence the ligand did not significantly change the mechanical stability of the pseudoknot. The average force for unfolding the alternate structure (~ 16 pN) was also unchanged within error, as was the ΔL_c for the alternate structure (all results listed in Table 3.1).

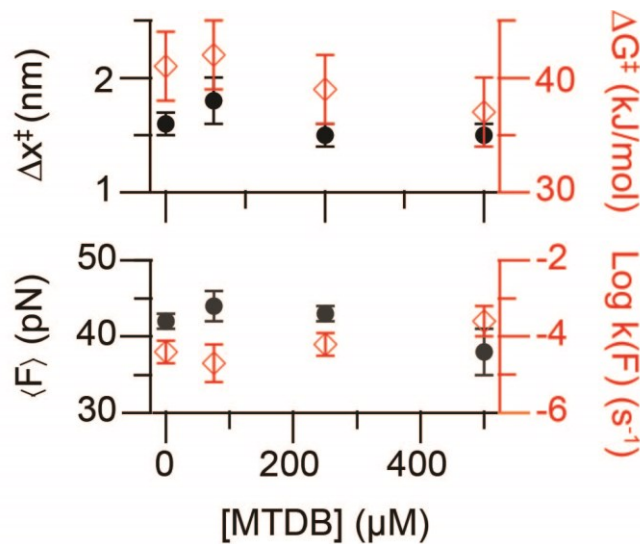


Figure 3.5: The average unfolding force (upper panel, black) and zero-force unfolding rate (upper panel, red), as well as the position (lower panel, black), and height (lower panel, red) of the barrier for unfolding, were all unchanged by ligand binding.

[MTDB] (μM)	0	75	250	500
Number of curves	881	624	1295	1171
% alternate	30 ± 3	24 ± 3	13 ± 1	8 ± 1
ΔL_c native (nm)	33 ± 1	34 ± 1	33 ± 1	32 ± 1
$\langle F \rangle$ alt. (pN)	42 ± 1	44 ± 2	43 ± 1	38 ± 3
$\log k_o$ (s^{-1})	-4.4 ± 0.3	-4.7 ± 0.5	-4.2 ± 0.3	-3.6 ± 0.4
$\Delta\lambda^\ddagger$ (nm)	1.6 ± 0.1	1.8 ± 0.2	1.5 ± 0.1	1.5 ± 0.1
ΔG^\ddagger (kJ/mol)	41 ± 3	42 ± 3	39 ± 3	37 ± 3
ΔL_c alt. (nm)	21 ± 1	22 ± 1	21 ± 1	20 ± 1
$\langle F \rangle$ alt. (pN)	16 ± 1	16 ± 1	14 ± 1	17 ± 1

Table 3.1: Summary of results

However, the fraction of FECs showing unfolding from the alternate structure was progressively reduced at increasing ligand concentrations, from 30 ± 3 % without ligand to 8 ± 1 % at $500 \mu\text{M}$. Representative unfolding force distributions are shown in Figure 3.6 at $250 \mu\text{M}$ MTDB, for the native (black) and alternate (blue) structures.

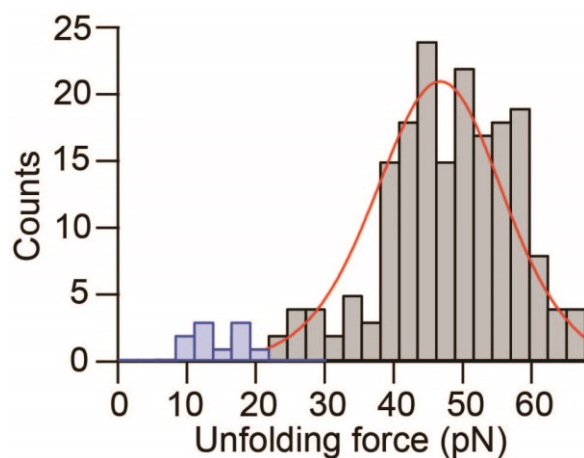


Figure 3.6: The unfolding force distribution in the presence of $250 \mu\text{M}$ ligand showed a reduction in the extent of alternate structure formation.

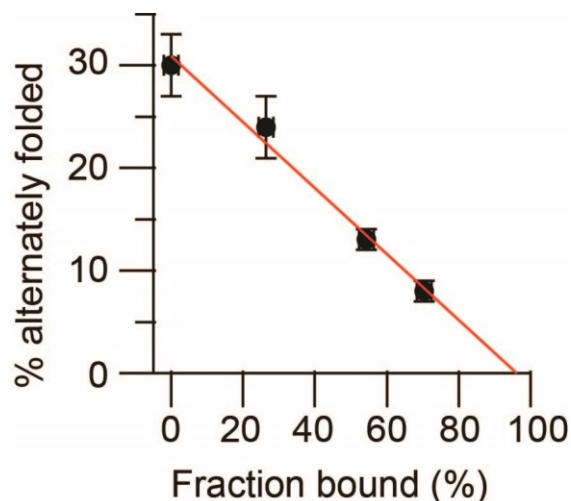


Figure 3.7: The extent of alternate structure formation dropped linearly with the fraction of pseudoknots that were bound by ligand.

Inferring from $K_d = 210 \mu\text{M}$ the fraction of ligand-bound pseudoknots (Ritchie et al., 2014), we found that the prevalence of the alternate structure varied linearly with the fraction of pseudoknot bound (Figure 3.7). From the linear fit, the incidence of alternate structures goes to zero when $96 \pm 8 \%$ pseudoknots are bound, indicating that ligand binding effectively eliminates the formation of alternate structures. This reduction in alternate structure formation mirrors the suppression of -1 PRF efficiency caused by the ligand, which was found to reduce -1 PRF to near-background levels (Park et al., 2011).

3.3 Discussion

A model for MTDB binding to the SARS pseudoknot was proposed previously based on docking calculations (Park et al., 2011). In this model, MTDB forms hydrogen bonds with nucleotides in loop 3, which bridges the junction between

stems 2 and 3 (Figure 3.1). Only a few bonds to the RNA were proposed in the model, consistent with the relatively weak binding we found. Interestingly, the junction where binding is thought to occur contains nucleotides that are susceptible to cleavage by probes sensitive to both double- and single-stranded RNA, indicating that the junction is flexible and exists in a dynamic conformational equilibrium (Su et al., 2005).

Such a picture is also consistent with our results, which suggest that MTDB binds to a flexible region of the SARS pseudoknot, thereby stabilizing it conformationally. Analogous behavior is seen in riboswitches, where ligand binding greatly reduces the conformational flexibility of the RNA (Serganov and Patel, 2012), although in the case of riboswitches the ligand binding usually enhances the mechanical stability of the structure significantly, as well (Greenleaf et al., 2008; Neupane et al., 2011). A crucial contrast here is that the ligand does not significantly increase the mechanical stability of the pseudoknot structure. Indeed, the observation that a pseudoknot-binding ligand that suppresses -1 PRF does not significantly alter the mechanical stability of the pseudoknot, but does suppress its ability to sample multiple structures, provides further evidence against the view that pseudoknot mechanical stability determines -1 PRF efficiency (Chen et al., 2009; Hansen et al., 2007). Instead, it reinforces the notion that the conformational plasticity and dynamic characteristics of the pseudoknot play an important role (Houck-Loomis et al., 2011; Ritchie et al., 2012; Wang et al., 2002). We thus propose a mechanism whereby MTDB binding reduces SARS CoV -1 PRF efficiency by reducing the conformational plasticity of the SARS pseudoknot, consistent with our previous work highlighting an under-

appreciated role for pseudoknot structural dynamics in regulating -1 PRF levels (Ritchie et al., 2012).

How might pseudoknot structural dynamics help determine -1 PRF efficiency? The ribosome actively generates tension in the mRNA as structure is unfolded (Qu et al., 2011), suggesting that a dynamic conformational equilibrium could cause fluctuations in this tension which, when communicated to the tRNA-mRNA complex, lead to a frameshift (Ritchie et al., 2012). This picture is consistent with a previous proposal that refolding of a partially-unfolded pseudoknot during accommodation might induce a frameshift by pulling back on the mRNA (Plant and Dinman, 2005). It is also supported by evidence of dynamic structural fluctuations in pseudoknots that stimulate -1 PRF efficiently: pseudoknot structures with a relatively high frequency of base-pair breathing at the junction of the two stems have been found to be more efficient -1 PRF stimulators than more conformationally rigid pseudoknots (Wang et al., 2002).

Given the many elements involved in -1 PRF, MTDB could also modulate frameshifting through effects other than changes in the pseudoknot structural dynamics. For example, the ribosome interacts with the pseudoknot during frameshifting in a variety of ways, which might be affected by MTDB binding. Structural and functional studies suggest that triplex structures and exposed loop nucleotides may make or direct specific contacts to the ribosome that affect -1 PRF efficiency, possibly explaining why the efficiency can be reduced by removing or altering these structures (Chen et al., 2009, 1995; Cornish et al., 2005; Kim et al., 1999; Liphardt et al., 1999; Olsthoorn et al., 2010; Shen and Tinoco, 1995).

MTDB binding might prevent such specific interactions needed to promote -1 PRF via protection, steric clash, or stabilization of a non-functional pseudoknotted conformation, or it might create new interactions leading to increased proofreading. The ribosomal helicase also interacts generically with the mRNA structures it unwinds, to facilitate the melting process (Qu et al., 2011), possibly biasing the dynamic equilibrium in favor of certain structures or speeding up equilibration rates. MTDB binding to the pseudoknot might modulate the interactions mediating this active unwinding of mRNA structure, thereby affecting the coupling of structural dynamics and interactions with the ribosome that are important for regulating -1 PRF efficiency.

However, the fact that -1 PRF efficiency is correlated with conformational plasticity when varying two completely independent aspects of the measurement (anti-frameshifting ligand binding, in contrast to identity of the pseudoknot used to stimulate frameshifting (Ritchie et al., 2012)) is highly suggestive that the correlation reflects an actual mechanistic feature of -1 PRF common to all the measurements, rather than some artifact. Moreover, using ligand binding to alter -1 PRF efficiency as we have done here, as opposed to making mutations in the pseudoknot (Chen et al., 2009, 1995; Cornish et al., 2005; Kim et al., 1999; Liphardt et al., 1999; Olsthoorn et al., 2010; Shen and Tinoco, 1995) or comparing pseudoknots from different species (Ritchie et al., 2012), allows a more controlled study of the relationship between these structures and -1 PRF efficiency, since comparisons can be made for identical RNA molecules.

It is interesting to note that one of the challenges in building models of -1 PRF has been reconciling, within a single mechanistic framework, the seemingly disparate characteristics that appear to play important roles during frameshifting.

While much work remains before a complete model of -1 PRF can be realized, the observation of a correlation between -1 PRF efficiency and formation of alternate conformations across an increasing range of conditions suggests that conformational plasticity may be a common feature linking various frameshift signals, highlighting its importance as a determinant of -1 PRF efficiency.

4 Mechanical Models for Constant Force Measurements

4.1 Motivation

The overall fluctuations as observed in constant force data involve the accumulation of random movements by each component in the construct. As discussed in chapter 1 and 2, the molecule's conformational fluctuation can be viewed as a diffusive process over its energy landscape, with the fluctuation rates set by a diffusion coefficient. Note that the diffusion coefficient here does not relate to the translational mobility, but rather the “conformational mobility” that characterizes how fast the molecular structure changes. On the other hand, the stiffness of a molecule can be extracted from equilibrium measurements because it is directly related to the fluctuation timescale. This information is of interest because it provides insight into the conformational dynamics of the molecule.

The conformational dynamics of the molecule itself are hidden in the measured signals due to the simultaneous movements of beads and handles. Unfortunately, the serially connected construct cannot be represented by a linear system, in which the superposition principle can be conveniently applied. In light of this, Hinczewski and colleagues have developed a dynamic deconvolution theory that aims to recover the dynamical properties of bio-molecules in the context of optical tweezers experiments (Hinczewski et al., 2010).

It is important to note the difference between the dynamic information extracted from molecules of interest within the tweezers measurements, as opposed to molecules in isolation. Considering that a molecule in a measurement

like the one shown in Figure 2.1 will be affected by the viscous drag of the beads and handles, its dynamic properties will be different than those in isolation. This kind of information is certainly less interesting, as molecules are never connected to polystyrene beads *in vivo*. Thus, a successful deconvolution theory should be able to extract, for example, the diffusion coefficient and stiffness of a protein as if they are in isolation.

Eventually we hope to develop a general mechanical model describing each component and its fluctuation timescale with different parameters. As constant force measurements are often bandwidth limited by factors such as bead sizes and length of handles, we need a model capable of predicting these effects on the conformational dynamics of proteins, and of probing the limit when the information is completely buried. Understanding the mechanics of bead and handle fluctuation can help us differentiate the real response of proteins from noise.

4.2 Dynamic Deconvolution of a Network

This section presents and expands up on the work by Hinczewski and colleagues (Hinczewski et al., 2010). Using the framework developed by the authors for a dual-trap measurement, we extended some of their results to accommodate for the fact that our optical tweezers setup is not symmetrical (with different handle sizes, bead sizes, and trap stiffness). Unless otherwise stated, the equations are mostly derived directly from Hinczewski's paper.

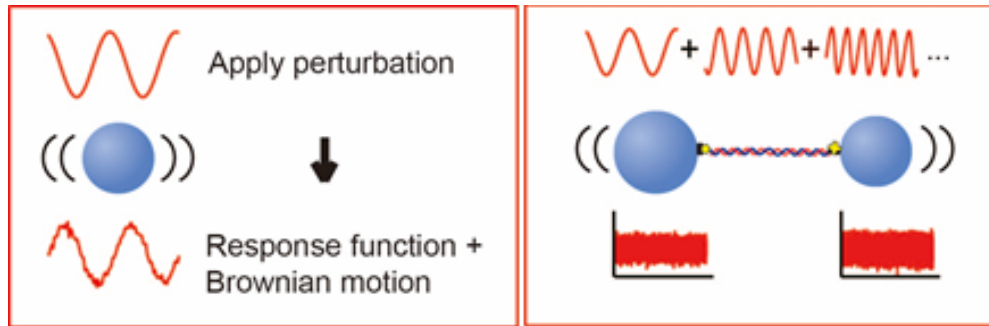


Figure 4.1: The force perturbation acting on the bead, generating a response from the bead movements. The overall response is the convoluted sum of each frequency components.

The derivation of the dynamic deconvolution theory stems from a Fourier analysis of the motions of each component in the system. Consider a bead where an oscillatory force along the pulling axis is applied; the position fluctuation of the bead will exhibit a response of the same frequency, but with a different amplitude, coupled by additional random motions as a result of thermal energy. Since any time series can be expressed as a sum of a Fourier series, the overall response of the system can be viewed as the convoluted sum of response of the system at each frequency (Figure 4.1). It is therefore much easier to apply deconvolution to a signal in frequency space instead of time space.

The linear response of an object, $J(\omega)$, under a stretching force in optical tweezers is defined as the ratio of the complex amplitude of its position fluctuation, $z(\omega)$, and the force, $f(\omega)$, it experiences.

$$J(\omega) = \frac{z(\omega)}{f(\omega)} \quad [4.1]$$

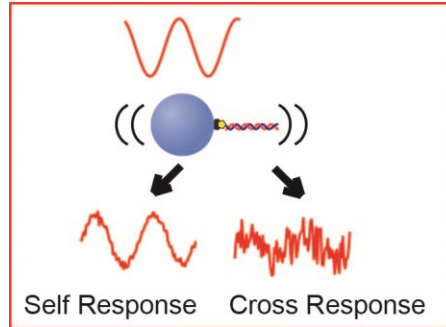


Figure 4.2: The general notion of self and cross responses. They refer to the response of handle or proteins occurring at the same and the opposite side of the applied force, respectively.

Consider a partial construct where the force is applied from one end (Figure 4.2). The self and cross response of the construct correspond to movements on the same and the opposite side of the applied force, respectively. In general, responses can be asymmetrical, but symmetric assumptions on the handle's and protein's response function can greatly simplify the set of deconvolution equations.

After introducing the notion of self and cross individual responses, we need to build the total response function from the bottom up by combining the responses from each mechanical element in the measurement. The general nomenclature for composite responses, when two components are connected, is J_i^A . The superscript denotes the components whose motions are described by the response function, while the subscript i denotes either the self or cross response.

A two component composite response is derived by considering two objects, A and B, connected by an imaginary spring of stiffness γ . When an

oscillatory force $f_L e^{-i\omega t}$ is applied from the left end of A, the resulting fluctuation along the pulling axis, z_{AL} , becomes:

$$z_{AL} = J_{self,L}^A f_L + J_{cross}^B f \quad [4.2]$$

where $f = -\gamma(z_{AR} - z_{BL})$ denotes the instantaneous force exerted by the imaginary spring, with z_{AR} and z_{BL} referring to the fluctuations of the right end of component A and the left end of component B, respectively. On the other hand, Newton's third law implies the following set of equations:

$$z_{AR} = J_{cross}^A f_L + J_{self,R}^A f \quad [4.3]$$

$$z_{BL} = -J_{self,L}^A f \quad [4.4]$$

$$z_{BR} = -J_{cross}^B f \quad [4.5]$$

By definition, the composite responses are:

$$J_{self,A}^{AB} = \frac{z_{AL}}{f_L} \quad [4.6]$$

$$J_{self,Y}^{AB} = \frac{z_{BR}}{f_R} \quad [4.7]$$

$$J_{cross}^{AB} = \frac{z_{BR}}{f_L} = \frac{z_{AL}}{f_R} \quad [4.8]$$

It is relatively straightforward to derive the remaining equations for forces applied from the right. Thus, by taking the imaginary spring stiffness to the limit of $\gamma \rightarrow \infty$, we can solve for the full response function.

$$J_{self,A}^{AB} = J_{self,L}^A - \frac{(J_{cross}^A)^2}{J_{self,R}^A + J_{self,L}^B} \quad [4.9]$$

$$J_{cross}^{AB} = \frac{J_{cross}^A J_{cross}^B}{J_{self,R}^A + J_{self,L}^B} \quad [4.10]$$

$$J_{self,B}^{AB} = J_{self,R}^B - \frac{(J_{cross}^B)^2}{J_{self,R}^A + J_{self,L}^B} \quad [4.11]$$

Equations 4.9-4.11 form the basis of the dynamic deconvolution theory. The total response for a network of three or more components can be found by reiterating the convolution rules.

The remaining piece is the problem of calculating the total response function from time series measurements of bead fluctuations. The key to this problem is the use of the Fluctuation-Dissipation Theorem (FDT). The spontaneous fluctuation of a system under random thermal motion is fundamentally related to its response to an external perturbation. The Langevin theory of Brownian motion, along with results from the Einstein-Smoluchowski equation, yield an equation that relates the diffusion coefficient, D of an object to its mobility, μ :

$$D = \mu k_B T \quad [4.12].$$

Equation 4.12, called the Einstein relation, connects the coefficient of diffusion with the mobility of the system, and it implies that the ultimate source of diffusion lies in the random, fluctuating force arising from the incessant motion of the fluid molecules (Pathria and Beale, 2011).

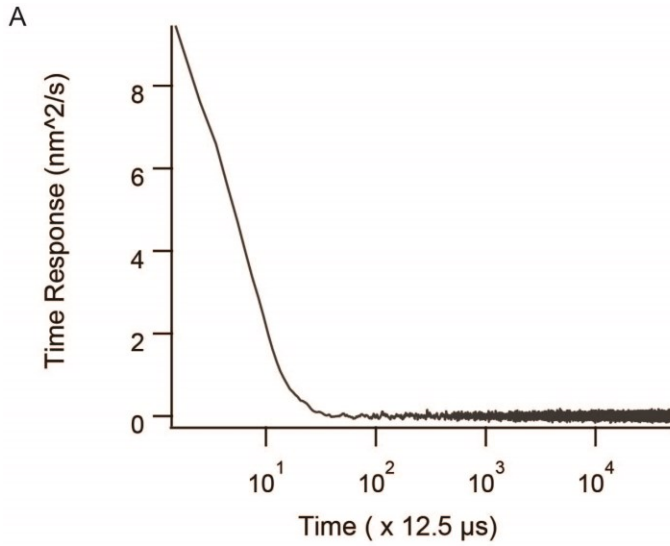
The diffusion coefficient is a measure that relates an object's displacement to the driving force of diffusion arising from thermal energy or electrochemical potential. Loosely speaking, the diffusion coefficient can be seen as a particle's

ability to diffuse through a fluid. On the other hand, the mobility μ comes from the notion of viscous drag, which determines the velocity of a particle in fluid when it is propelled by an external force.

The FDT establishes the fundamental relationship between the mobility, which represented the dissipative force of the system, and the autocorrelation function of the fluctuations (Pathria and Beale, 2011). It can be deduced from the FDT that the derivative of an autocorrelation function of a time series is equivalent to its time domain linear response, differing only by the Boltzmann factor $k_B T$ (Landau and Lifshitz, 1996). A common definition for the autocorrelation of a time series, $R(\tau)$, is given by:

$$R(\tau) = \langle z(t + \tau)z(t) \rangle \quad [4.13]$$

Direct calculation using equation 4.13 is certainly possible, but it is computationally intensive. As an alternative, we invoke the Wiener-Khinchin theorem, which states that the autocorrelation function is equivalent to the Fourier transform of the absolute square of the time series (Cohen, 1992). To obtain the time and frequency domain response, we can take the derivative of the autocorrelation function and consequently its Fourier transform. As seen in Figure 4.3b, the raw Fourier Transform of a time response function exhibits high frequency noise contamination. This is due to the fact that the statistics are insufficient for the higher time lag calculation of autocorrelation. The number of discrete frequency components depends on the number of points in time series used for Discrete Fourier Transform calculations (Smith, 2007). We can overcome this artifact by filtering the frequency domain response with log scale averaging, such that the bins size are equal in the logarithmic scale (Figure 4.3c).



:

Figure 4.3(a): The time space response obtained by differentiating the mean square displacement of the bead position.

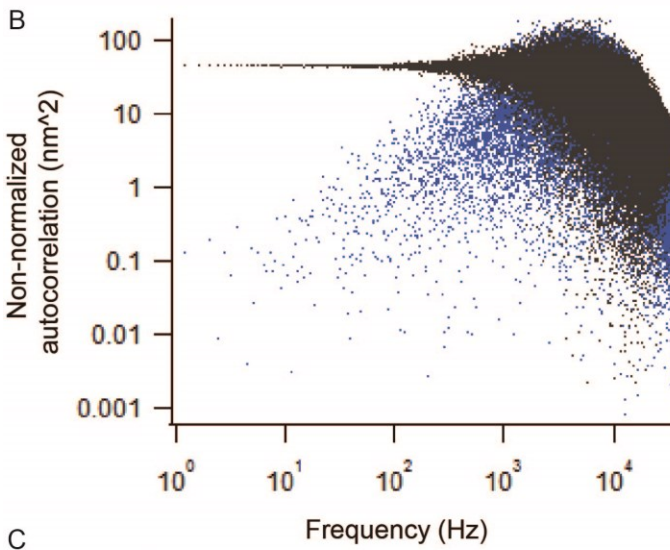


Figure 4.3(b): The raw frequency space response by applying Fourier Transform directly.

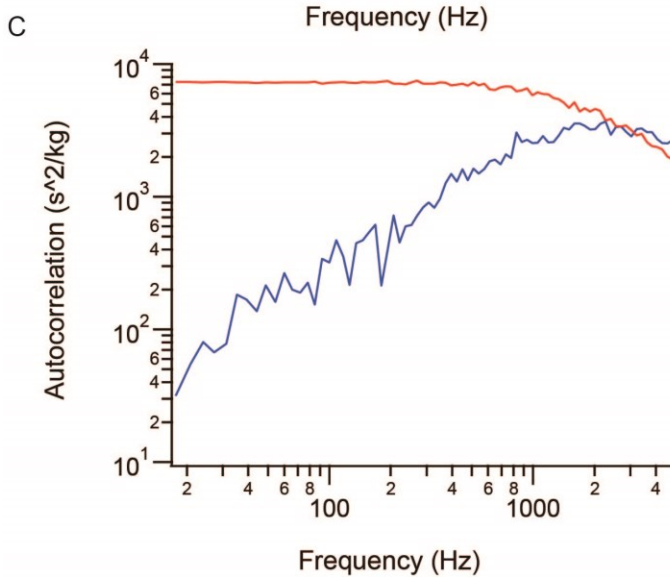


Figure 4.3(c): The filtered frequency space complex response. (Blue denotes the real part, and red denotes the imaginary part)

As a summary, given a set of position measurements (Figure 4.4a), we will calculate its autocorrelation function by applying the Wiener-Khinchin Theorem (Figure 4.4b); to obtain its time/frequency domain response (Figure 4.4c,d).

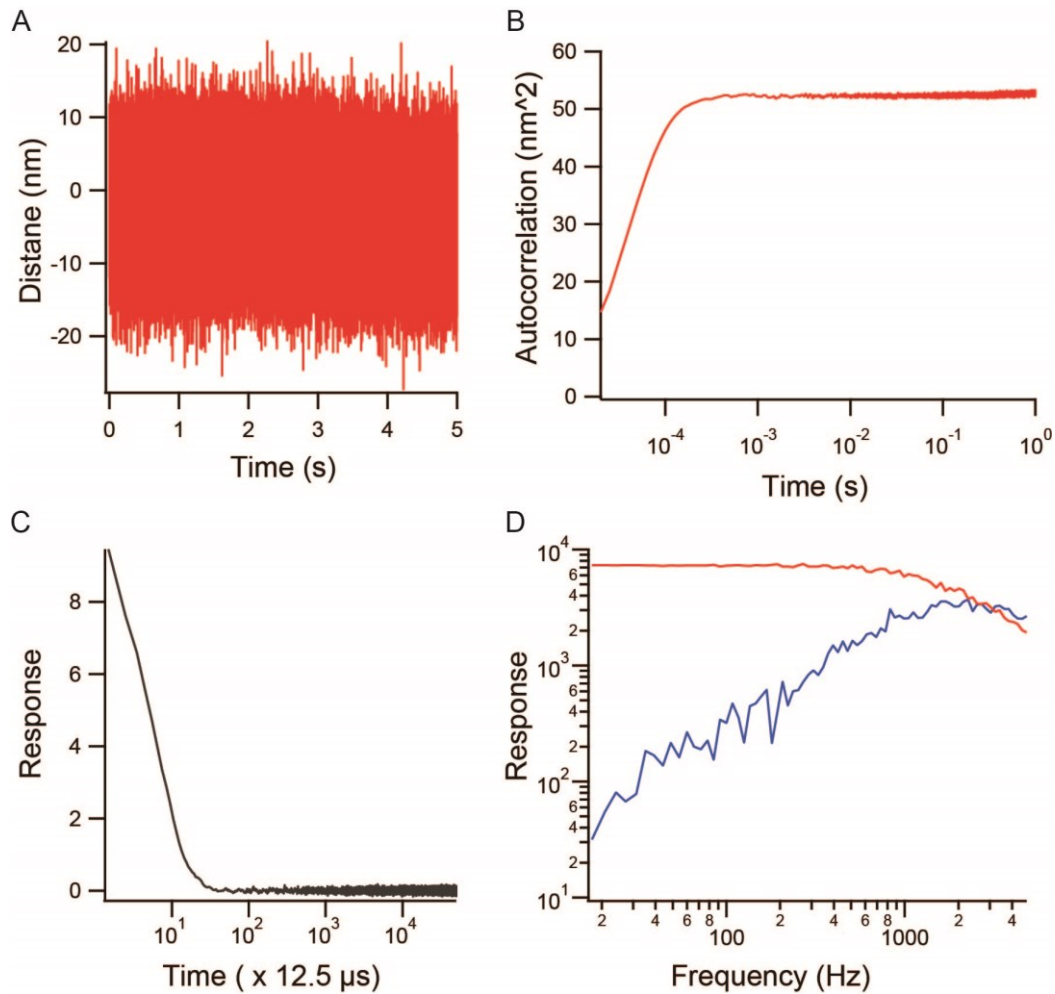


Figure 4.4: (a) The raw data as measured in constant force experiments. (b) The autocorrelation function calculated using the Wiener-Khinchin Theorem. (c) The time space response obtained by differentiating the autocorrelation function. (d) The filtered frequency space response. (Blue denotes the real part, and red denotes the imaginary part)

We are eventually interested in the individual response of a protein. However, the total response is not an explicit function of the protein's response. Direct inversion will lead to instabilities in the solution for the protein's response function because the Fourier transform of the total response can contain noise that leads to asymptotic behavior. A more feasible approach is to model the functional form of the bead response using the FDT, and the handle response using results from the worm-like chain (WLC) model. We first build the network bottom up by combining the theoretical functional forms via the set of convolution equations 4.9-4.11. The model is then fitted to the total response calculated from experimental time series, yielding parameters that characterize the individual responses. Details on each response function will be discussed in Chapter 5.

5 Dynamic Deconvolution of Experimental Data

In Chapter 4 we discussed how the response of a network of mechanical components can be built from the bottom up if the response function of each component is known. The functional form of the bead and handle response can be derived using the FDT and the WLC models, respectively. In this chapter, we want to test the validity of both the response functions and the deconvolution approach through a series of measurements using different constructs: beads only, beads with DNA handles, and beads with DNA handles linked to a protein molecule.

5.1 Bead Measurements

A bead's motion in an optical trap can be modelled as a diffusive Brownian particle constrained as an oscillator in a harmonic potential. By extending the Langevin theory of Brownian motion to include a harmonic term with a spring constant k^{Trap} , we can write the one-dimensional equation of motion (Equation 5.1):

$$m \frac{d^2 x}{dt^2} + \frac{1}{\mu^B} \frac{dx}{dt} + k^{Trap} x = F(t) \quad [5.1]$$

Here μ^B is the mobility of a spherical particle in a fluid with viscosity η , k^{Trap} is the stiffness of the optical trap, $F(t)$ is the time-dependent external force, and m is the mass of the particle.

The solution to the differential equation can be found by decomposing the response into a sum of independent terms involving a sinusoidal applied force (Hinczewski et al., 2010; Pathria and Beale, 2011). As a result, the response function of a single bead in frequency space takes the form of a Lorentzian (Equation 5.2).

$$J_B(\omega) = \frac{\mu^B}{\mu^B k^{Trap} - i\omega} \quad [5.2]$$

In order to test the validity of this function, single bead experiments were performed with various trap stiffness and bead radii. The bead was trapped with a stiffness ranging from 0.1-0.2 pN/nm, and fluctuations in its position were measured and recorded as a function of time (Figure 5.1).

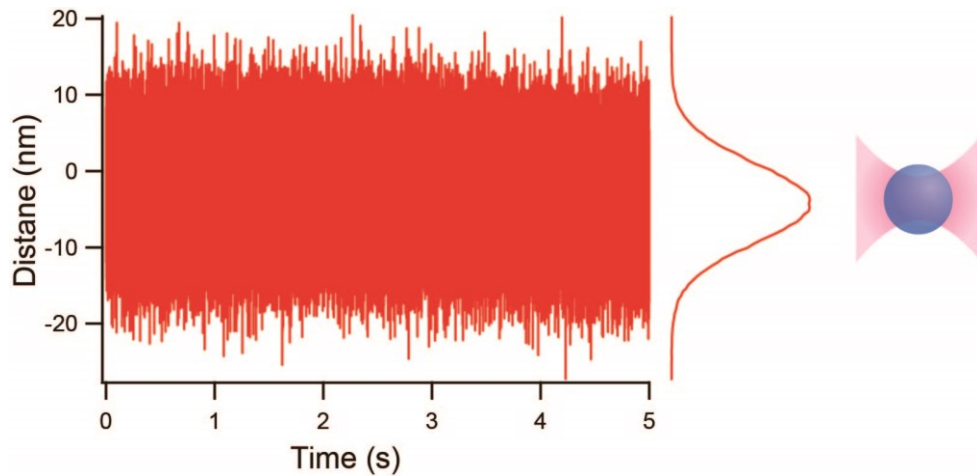


Figure 5.1: Sample data trace from single bead measurements. The position distribution is roughly Gaussian, as expected for a harmonic trapping potential.

The time traces can be analyzed using the procedural steps detailed in chapter 4. Figure 5.2 shows an example of the autocorrelation of a bead with radius 300 nm, and its corresponding filtered frequency space response with fits.

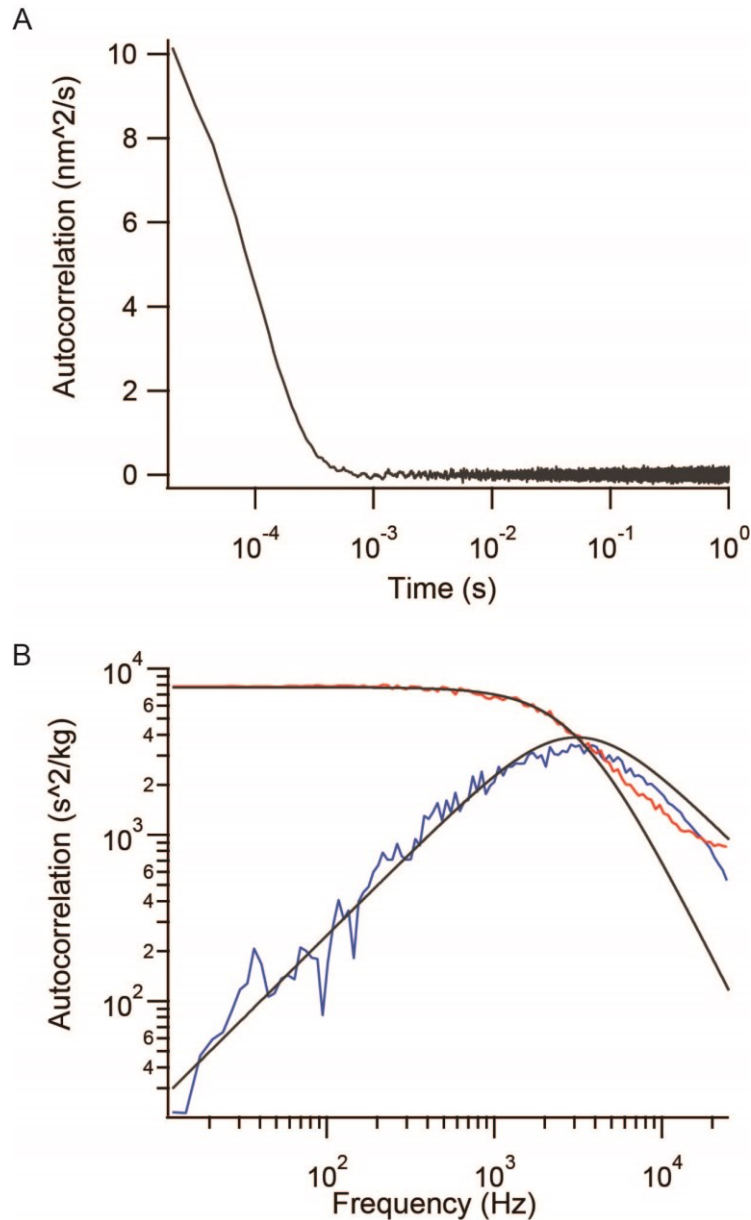


Figure 5.2: Position autocorrelation of a bead of radius 300 nm being held at a stiffness of 0.15 pN/nm. Bead response in (a) time space and (b) frequency space. Red and blue lines show the real and imaginary parts of the response, respectively. Black lines show the corresponding fits to the response using equation 5.2. The Lorentzian discrepancy occurs above 3 kHz.

As seen from Figure 5.2b, at frequencies above 3 kHz, the response starts to deviate from the characteristic $1/\omega^2$ drop of the Lorentzian function. The high frequency discrepancy suggests that the bead's movement during shorter time scale are highly correlated, and this discrepancy is most likely contributed by factors other than the bead dynamics. The Lorentzian is merely a simplistic first order approximation of the bead response. However, we will show in section 5.4 that the protein conformational dynamics can in fact be captured in the low frequency range, so that the deconvolution approach is still feasible by limiting the fit range.

As a first order approximation, we can fit the response with a frequency range constraint (<3 kHz) to extract the trap stiffness and bead mobility using equation 5.2. The extracted trap stiffness can be compared to other established ways to measure the trap stiffness, namely the power spectrum and variance methods (Berg-Sørensen and Flyvbjerg, 2004; Neuman et al., 2007). Figure 5.3 shows that the trap stiffness obtained from the autocorrelation method agrees well with the results from the variance and the power spectrum methods. To estimate the bead radius correctly, we need to invoke Faxen's correction of Stokes' law, a phenomenological description (equation 5.3) for the diffusion of spherical particles near a surface (Viana et al., 2007). The correction is necessary because the beads are trapped roughly a diameter (600 nm) away from the surface, making the proximity effect significant. Here $\eta = 10^{-3}$ Pa.s is the viscosity of water at 20° C, r is the bead radius, and h is the distance of bead center from the surface.

$$\mu_B = \frac{6\pi\eta r}{1 - \frac{9}{16}\left(\frac{r}{h}\right) + \frac{1}{8}\left(\frac{r}{h}\right)^3 - \frac{45}{256}\left(\frac{r}{h}\right)^4 + \frac{1}{16}\left(\frac{r}{h}\right)^5} \quad [5.3]$$

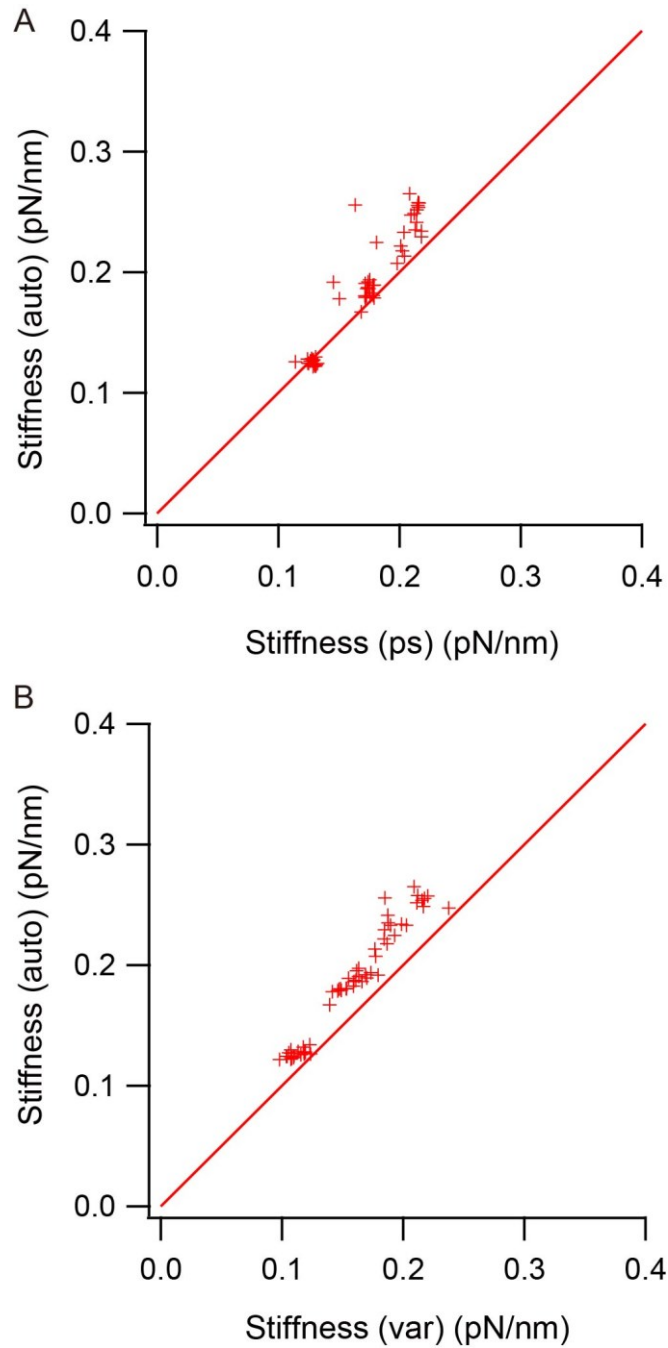


Figure 5.3: Stiffness comparison. Extracted stiffness are compared to other established stiffness measurement methods. (a) Stiffness measured using the autocorrelation and the power spectrum method (b) Stiffness measured using the autocorrelation and the variance method. Solid lines indicate the expected equality between the results from different methods.

Using equation 5.3, we obtained the following results: 268 ± 3 nm at 0.12 pN/nm, 283 ± 3 nm at 0.15 pN/nm, and 293 ± 5 nm at 0.19 pN/nm. These numbers are quite close to the nominal expected value of 300 nm. The discrepancy from the nominal value becomes smaller at higher trap stiffness, for reasons that are not yet understood. Note that the errors are reported as standard error of the mean.

5.2 Hydrodynamic Effect Measurements

Constant force experiments are usually done at a trap separation of 500-1000 nm, depending on the length of handle used. Since the beads are only 1 to 2 diameters apart, the hydrodynamic effect, or the vortex in a fluid generated by random bead movements, may be significant. At such a close distance, the turbulence of the fluid will affect the movement of the beads leading to additional noise in the bead's response function. In order to test whether there is a significant coupling between the motions of two beads, we designed a set of experiments that replicate the experimental conditions used in protein folding measurements. A larger bead is trapped at a constant stiffness of 0.3 pN/nm, while a smaller bead is trapped at various trap stiffness, in the range of 0.1 to 0.2 pN/nm. The experiment is repeated at different bead separations so that the hydrodynamic effect can be observed at different distances.

Figure 5.4 shows the time and frequency response of the 300 nm bead in the presence of the second bead. The frequency response is analogous to result from the single bead measurements. Figure 5.5 presents the extracted bead radii at various trap stiffness and separations, compared to the single bead result. We

observed that while the extracted radii exhibited a similar average value, the variance in the results was systematically higher when another bead was present. The results are summarized in Table 5.1, showing that the twin bead results are consistent with those calculated from single bead measurements.

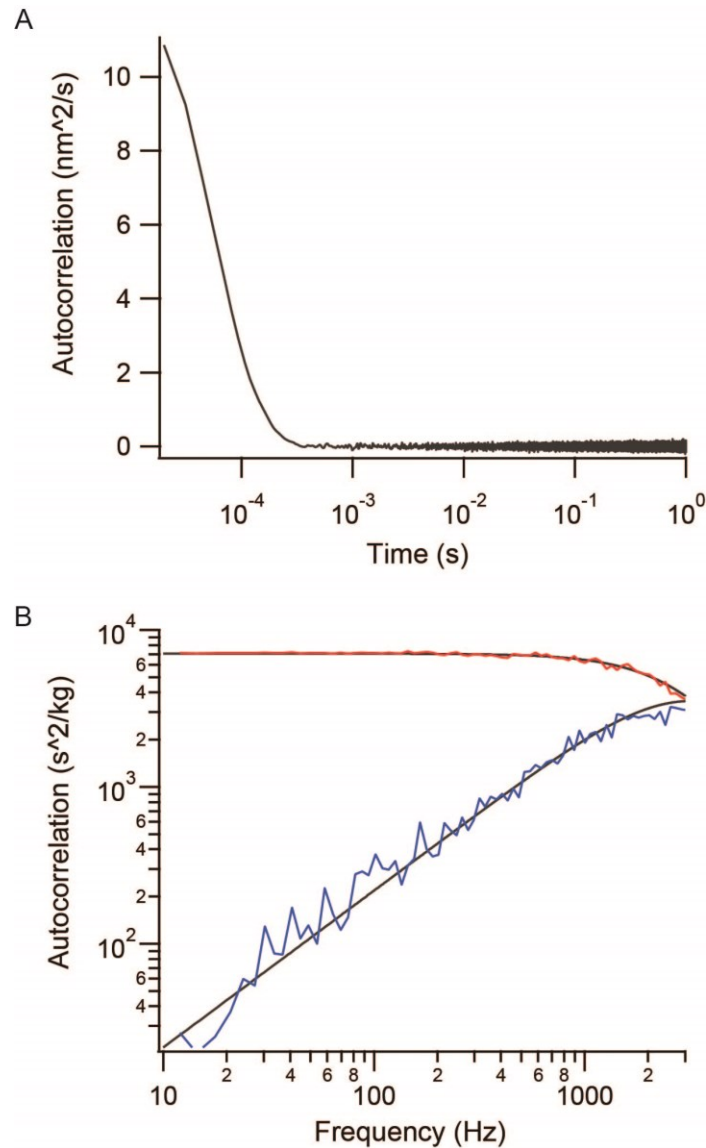


Figure 5.4: Position autocorrelation of a bead of radius 300 nm, being held with a stiffness of 0.15 pN/nm, but with the proximity of another bead of radius 410 nm, being held at 0.66 pN/nm. Bead response in (a) time space and (b) frequency space. Red and blue lines show the real and imaginary parts of the response, respectively. Black lines show the corresponding fits to the response using equation 5.2.

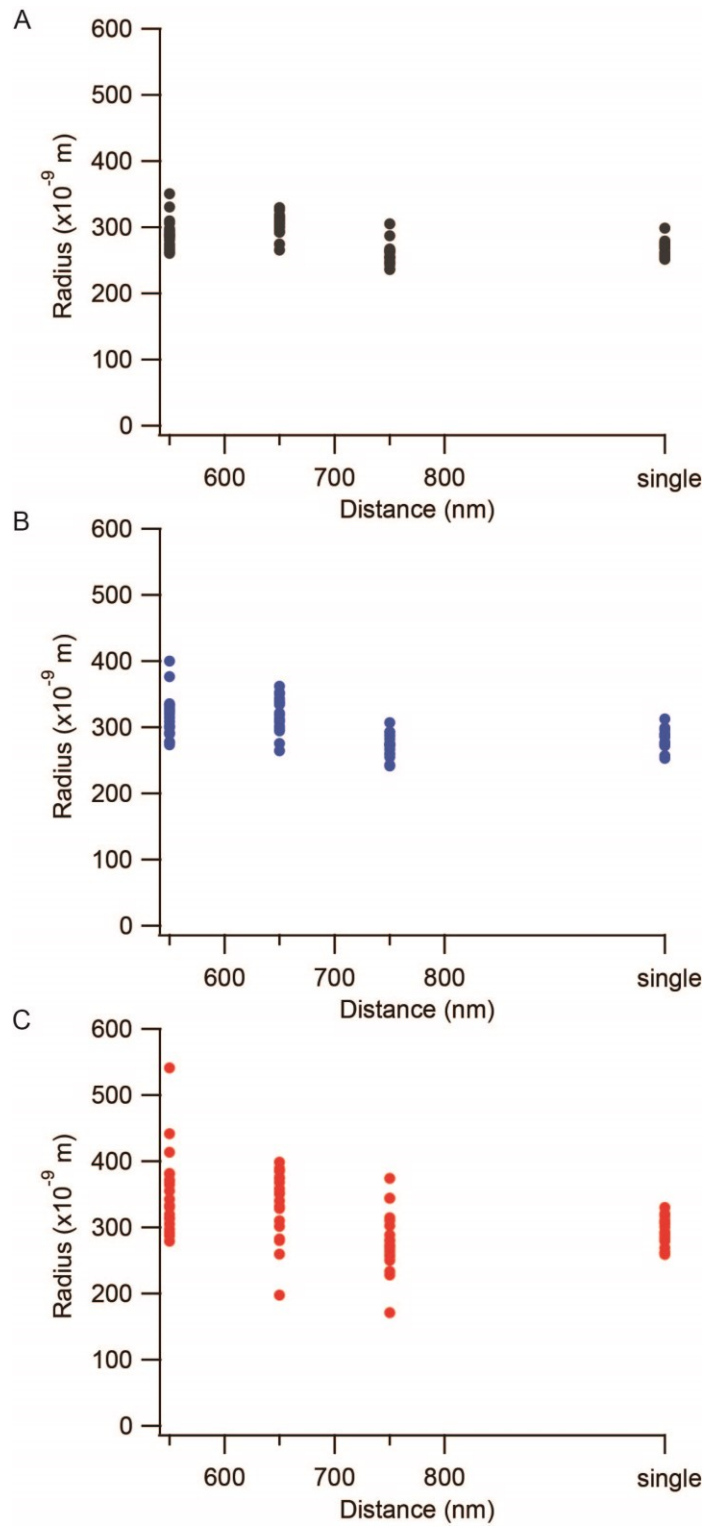


Figure 5.5: Summary of bead results. The bead radii are calculated using equation 5.3. A total of 20 beads are measured, being held at stiffness of (a) 0.12 pN/nm (b) 0.15 pN/nm (c) 0.19 pN/nm, respectively.

Distance\Stiffness	0.12 pN/nm	0.15 pN/nm	0.19 pN/nm
550 nm	289 ± 5 nm	315 ± 7 nm	352 ± 14 nm
650 nm	304 ± 4 nm	322 ± 6 nm	335 ± 12 nm
750 nm	259 ± 4 nm	273 ± 4 nm	280 ± 11 nm
single	268 ± 3 nm	283 ± 3 nm	293 ± 5 nm

Table 5.1: Summary of extracted bead radius results. Errors are reported as standard error of the mean.

5.3 Handle Measurements

Having measured the bead responses, we will now add in a handle to the construct. The next set of experiments will measure the overall tether-bead response, in the absence of protein. In the actual preparation of constructs, the tether is made by connecting two shorter handles, comprised of 1281 and 798 base-pairs, respectively, through a disulfide bond on one strand. The 1281-base-pair handle end is attached to the anti-digoxigenin functionalized bead of 410 nm radius, while the 798-base-pair handle end is attached to the avidin functionalized bead of 300 nm radius. This construct is held at a constant force with the smaller bead being pulled out of the center of the trap into the zero-stiffness region, and the larger bead trapped at a constant stiffness in the linear region (0.3 pN/nm). The same measurement was repeated at several different constant forces, ranging from 7 pN to 14 pN. Data were collected by Hao Yu between the months of May and June 2010.

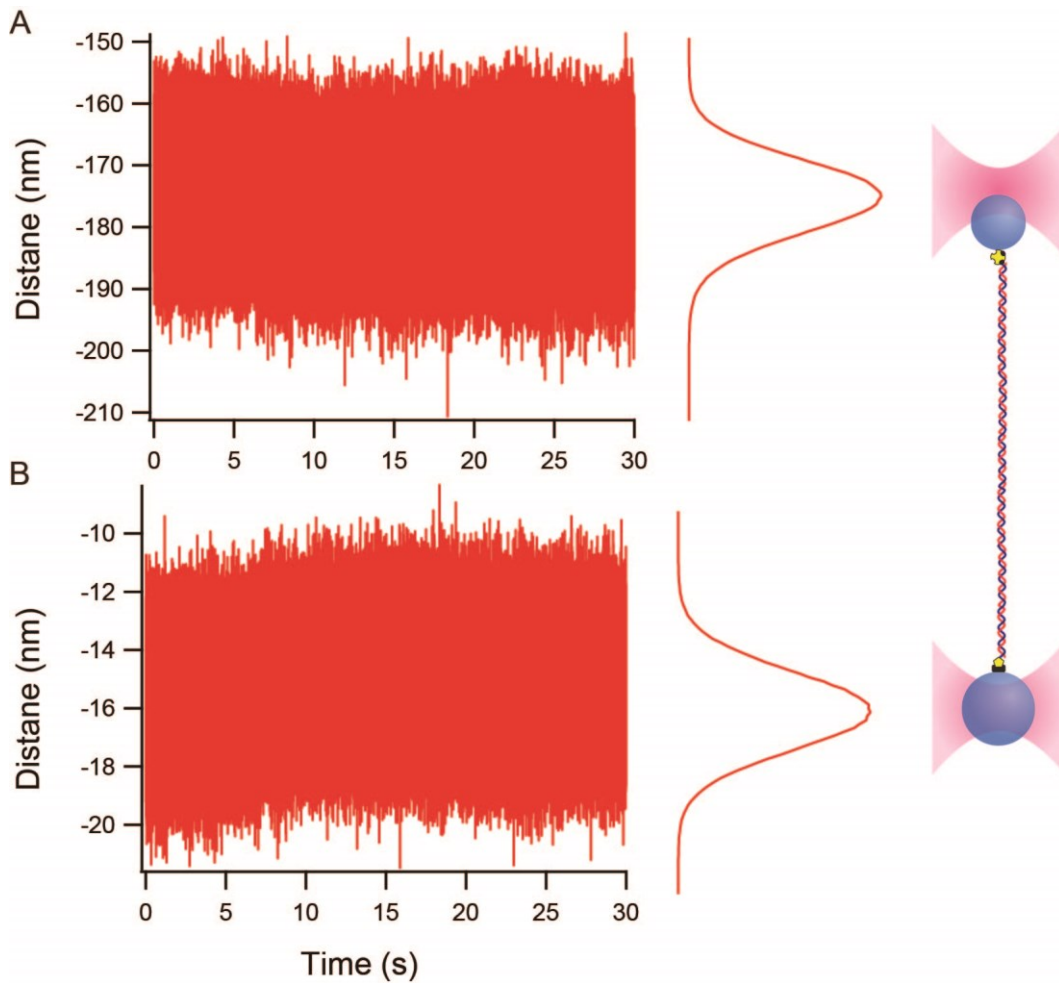


Figure 5.6: Sample data trace from handle measurements. (a) A 300 nm radius bead is trapped in the zero-stiffness region. (b) A 410 nm radius bead is trapped in the linear region.

Figure 5.6 shows the experiment setup schematic and a sample of data traces taken. Similar results were found from 2 different molecules, although the results are shown only for one.

Hinczewski and colleagues derived the expected functional form for the response of handles using the theory of polymer dynamics (Hinczewski et al., 2010). The key assumption in this derivation is that fluctuations along a semi-flexible polymer can be decomposed into a sum of normal modes. By assuming an

exponentially decaying autocorrelation function in time, the handle's normal mode response can be written as a sum of exponents, or as a sum of Lorentzians in frequency space. The sum of normal modes, with an additional center of mass term, can describe the response of handles completely (Equation 5.4 & 5.5).

$$J_{self}^H(\omega) = \frac{\mu_0^H}{-i\omega} + \sum_{n=1}^{Nmodes} \frac{\mu_n^H}{\mu_n^H k_n^H - i\omega} \quad [5.4]$$

$$J_{cross}^H(\omega) = \frac{\mu_0^H}{-i\omega} + \sum_{n=1}^{Nmodes} (-1)^n \frac{\mu_n^H}{\mu_n^H k_n^H - i\omega} \quad [5.5]$$

The normal modes can be arranged such that the $n = 1$ mode represents the mode with the largest relaxation time. To reduce the number of parameters necessary, we decided to fit the handle response by including only the first normal mode, because in the low temperature limit, the handle response is dominated by the center-of-mass term and the first normal mode. Hincewski proposed the addition of a term to describe the bead surface response (equation 5.6) when the bead is linked in a network. This additional term describes the contribution of the rotational motion of the bead, and it separates the response of the bead's surface from its center.

$$J_{surface}^B(\omega) = \frac{\mu^B}{\mu^B k^{Trap} - i\omega} + \frac{\mu_r^B}{\mu_r^B k_r^B - i\omega} \quad [5.6]$$

To extract the response for the handles alone, we need to build up the handle-bead network from its components. We can derive the response by first convoluting the two beads separately with their own handles, then combining them into a single entity. Unfortunately, the complete network now contains a total of 14 parameters, making overfitting of the data a concern. We find that an

unconstrained fit often leads to instabilities and asymptotic behaviour, because the minimization algorithm has to search through a 14-dimensional phase space, and any local extrema can cause the minimum searching process to fail. To overcome this difficulty, we constrained the handle parameters to values derived from the WLC model (Hinczewski et al., 2010). Equation 5.7 and 5.8 shows that the handle mobility should remain constant, while the handle stiffness should vary according to the 3/2 th power of force.

$$\mu_0^H \approx \mu_1^H = \frac{\ln\left[\frac{L}{\bar{a}}\right]}{2\pi\eta L} \quad [5.7]$$

$$k_1^H \approx \frac{4k_B T}{l_p L} \left(\frac{l_p F}{k_B T}\right)^{\frac{3}{2}} \quad [5.8]$$

The combined handle and beads' time and frequency responses are shown in Figure 5.7. By constraining the handle parameters (Figure 5.8), the corresponding fit result for bead parameters is shown in Figure 5.9.

The bead radii implied by the mobilities are 150 ± 50 nm and 530 ± 40 nm for the small and large bead, respectively. This is not unreasonable as the bead rotation is now coupled to the handle's fluctuation, causing the "effective" bead mobility to change. Another observation from Figure 5.8 is that the mobility of the smaller bead is varying with the applied force. This is consistent with the single bead results where the apparent bead radius seems to be increasing as we increase the trap stiffness.

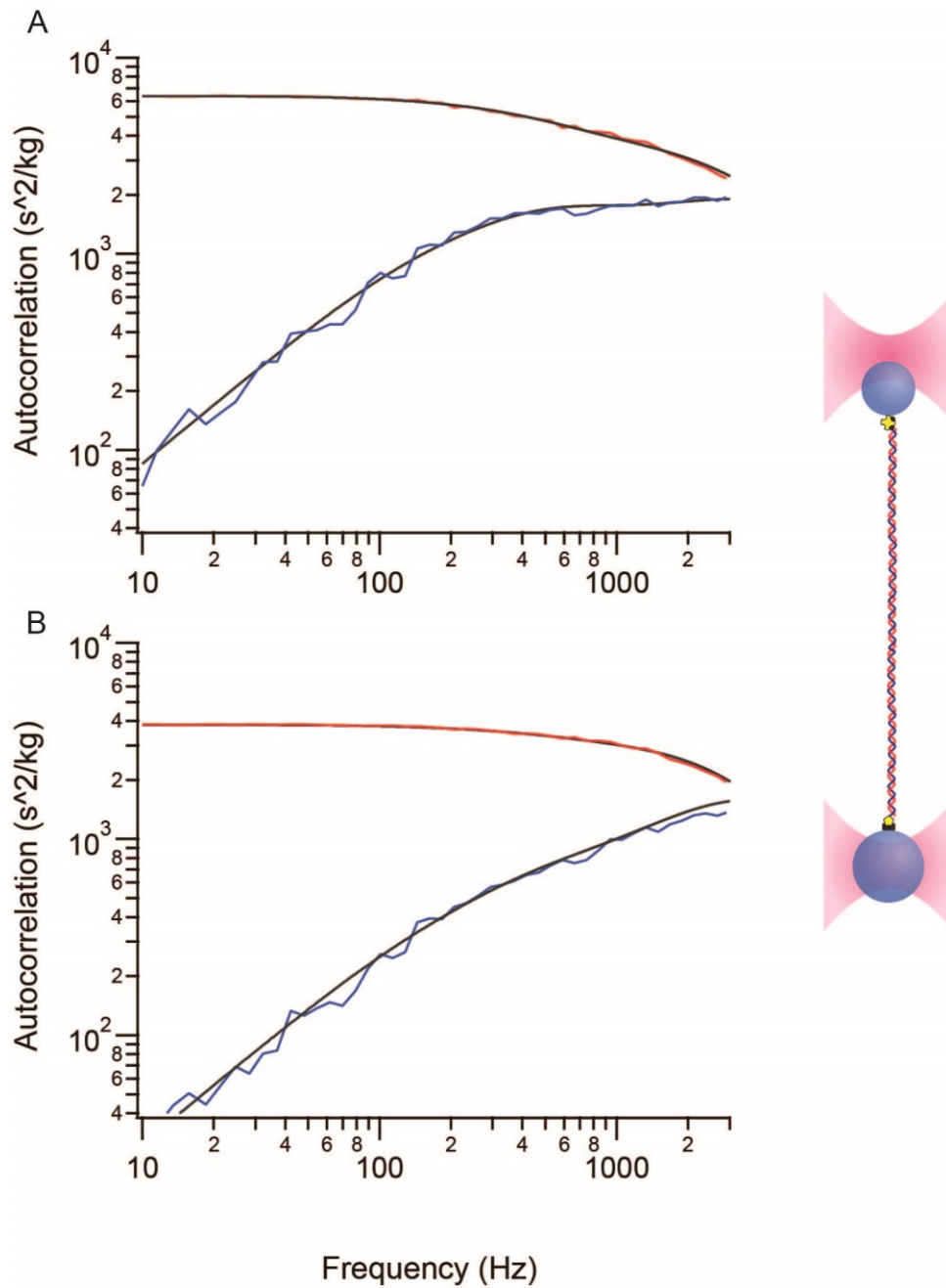


Figure 5.7: The position autocorrelation of a construct with handles being held at a constant force of 10.8 pN. The corresponding frequency response of the (a) 300 nm bead operating in the zero-stiffness region of the trap (trap 1) (b) 410 nm bead operating in the linear region of the trap (trap 2). Red and blue lines show the real and imaginary parts of the response, respectively. Black lines show the corresponding fits to the response functions.

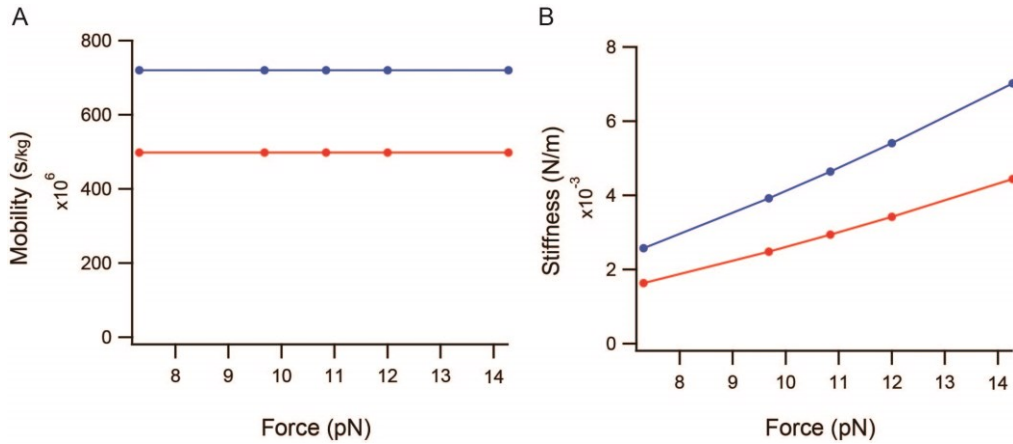


Figure 5.8: Constrained handle parameters using values estimated from the WLC model. Blue denotes the parameter of the handle being connected to the smaller bead while red denotes the parameter of the handle connected to the larger bead. Handle (a) mobility (μ_0^H/μ_1^H) (b) stiffness (k_0^H)

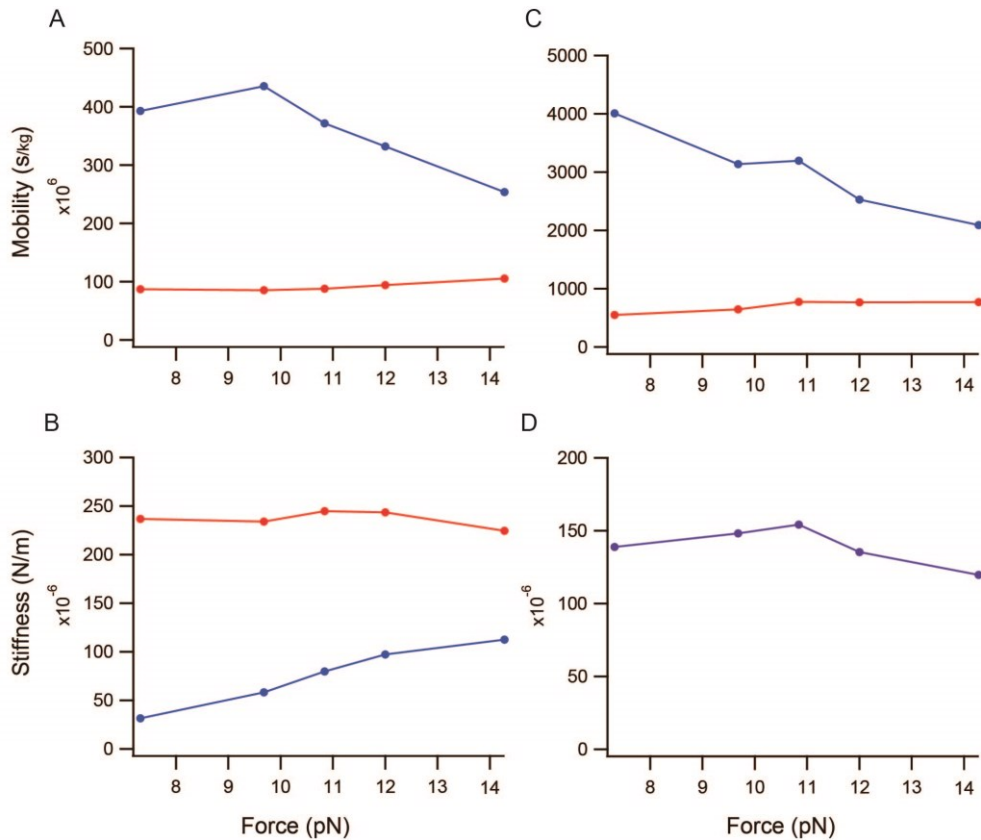


Figure 5.9: Extracted bead parameters. Blue and red denote the parameters that are related to the small and the large bead, respectively. Bead's (a) translational mobility (μ^B) and (b) rotational mobility (μ_r^B). (c) Trap stiffness (k^{Trap}) (d) Rotational elasticity (k_r^B). The rotational elasticity is the same for both beads.

5.4 Protein Measurements

After characterizing the response of the beads and handles, we can now proceed to measure a complete construct encompassing a protein. The protein used in our measurements is the recombinant Syrian hamster Prion Protein (SHaPrP, 90-231). The protein construct is prepared by first attaching it to the handles via disulfide bonds, then to the beads (Yu et al., 2012). The experimental setup for protein measurements is similar to the one outlined in the previous section. Data were collected by Hao Yu between the months of May and June 2010. Data is analyzed over 3 different molecules.

Hinczewski's paper derived the protein response function by using the numerical solution of the corresponding Fokker-Planck equation (Hinczewski et al., 2010). Assuming a double well potential and discretizing it over M values, they derived the generalized form of the protein response (Equation 5.10).

$$J^P(\omega) = \sum_{\alpha=1}^{M-1} \frac{\beta C_{\alpha} \Lambda_{\alpha}}{\Lambda_{\alpha} - i\omega} = \sum_{\alpha=1}^{M-1} \frac{\mu_{\alpha}^P}{\mu_{\alpha}^P k_{\alpha}^P - i\omega} \quad [5.10]$$

C_{α} and Λ_{α} are parameters related to the eigenvector and eigenvalue of the transition matrix of the discretized potential well (Hinczewski et al., 2010). The first Lorentzian of equation 5.10 models the potential as a well-defined parabolic well, while the remaining terms account for the anharmonic correction.

The authors proposed a key relation (Equation 5.11) that resembles the structure of equations 4.9 and 4.11.

$$J_{self}^{2HB+P} = 2J_{self,B}^{HB} - \frac{2(J_{cross}^{HB})^2}{J_{self,H}^{HB} + J^P/2} \quad [5.11]$$

Equation 5.11 assumes a symmetrical optical tweezers setup, which is not applicable in our case since we use different bead sizes and place them in different stiffness regions of asymmetrical traps. In view of that, we made a slight modification to the equation 5.11, where Hn and Bn (for $n = 1,2$) denote the responses respectively of the two handles and the two beads.

$$J_{self,Bn}^{2HB+P} = J_{self,Bn}^{HnBn} - \frac{(J_{cross}^{HnBn})^2}{J_{self,Hn}^{HnBn} + J^P/2} \quad n = 1,2 \quad [5.12]$$

We have already shown in section 5.2 that by constraining the handle parameters, we are able to obtain good fits with bead parameters consistent with the results from measurements of beads alone. We will employ the same strategy to extract the protein dynamics, using the first order term in equation 5.10.

As can be seen in Figure 5.10, the sample data trace shows how the protein can hop between different states. The distribution of states depends on the force exerted on the beads by the traps; higher force will push the protein to stay in the completely unfolded (higher extension) state and vice versa.

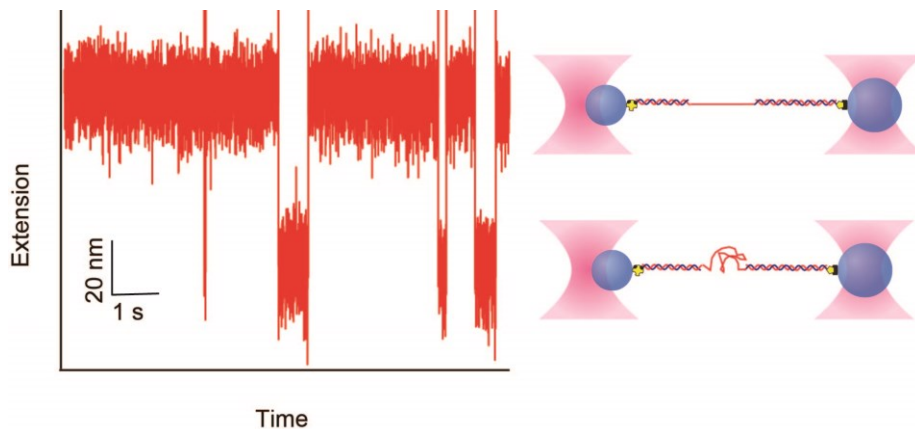


Figure 5.10: Sample data trace from handle measurements. The high extension state represents the completely unfolded molecule while the low extension state represents the folded molecule.

Figure 5.11 and 5.12 show the responses of the protein construct in the folded and unfolded states, respectively. We expanded on the data analysis procedure described in section 5.3, by adding in the protein's response function (5.10) to the convoluted network. We restricted the handle parameters to the values in Figure 5.8, while letting the beads and protein parameters to float freely. The corresponding fit results are summarized in Figure 5.13 and 5.14. Once we have found the protein's mobility from the fits, we can calculate the diffusion coefficient of the unfolded and folded states, respectively, from the mobility of protein (μ_{α}^P) using equation 4.12.

Analysing 51 data traces from 3 molecules, we found the diffusion coefficients of the completely unfolded and folded states to be $10^{-11.6 \pm 0.3}$ m²/s and $10^{-12.3 \pm 0.2}$ m²/s, respectively. Note that this diffusion coefficient relates to the diffusion of the protein over the conformational energy landscape along the reaction coordinate for folding (here, molecule extension), not merely the translation diffusion of the protein through the solution. The diffusion coefficient of our unfolded protein is consistent with previously values for conformational diffusion reported from fluorescence measurements, in the range 10^{-10} to 10^{-13} m²/s (Waldauer et al., 2010). It is remarkable that our results agree with the literature since fluorescence measurements do not typically involve beads and handles. In contrast, force spectroscopy measurements where the mechanical network was not deconvolved found much slower diffusion coefficients, 10^{-15} to 10^{-16} m²/s (Berkovich et al., 2012; Lannon et al., 2013). It is also important to note that this is the first time a diffusion coefficient has been calculated for a folded protein.

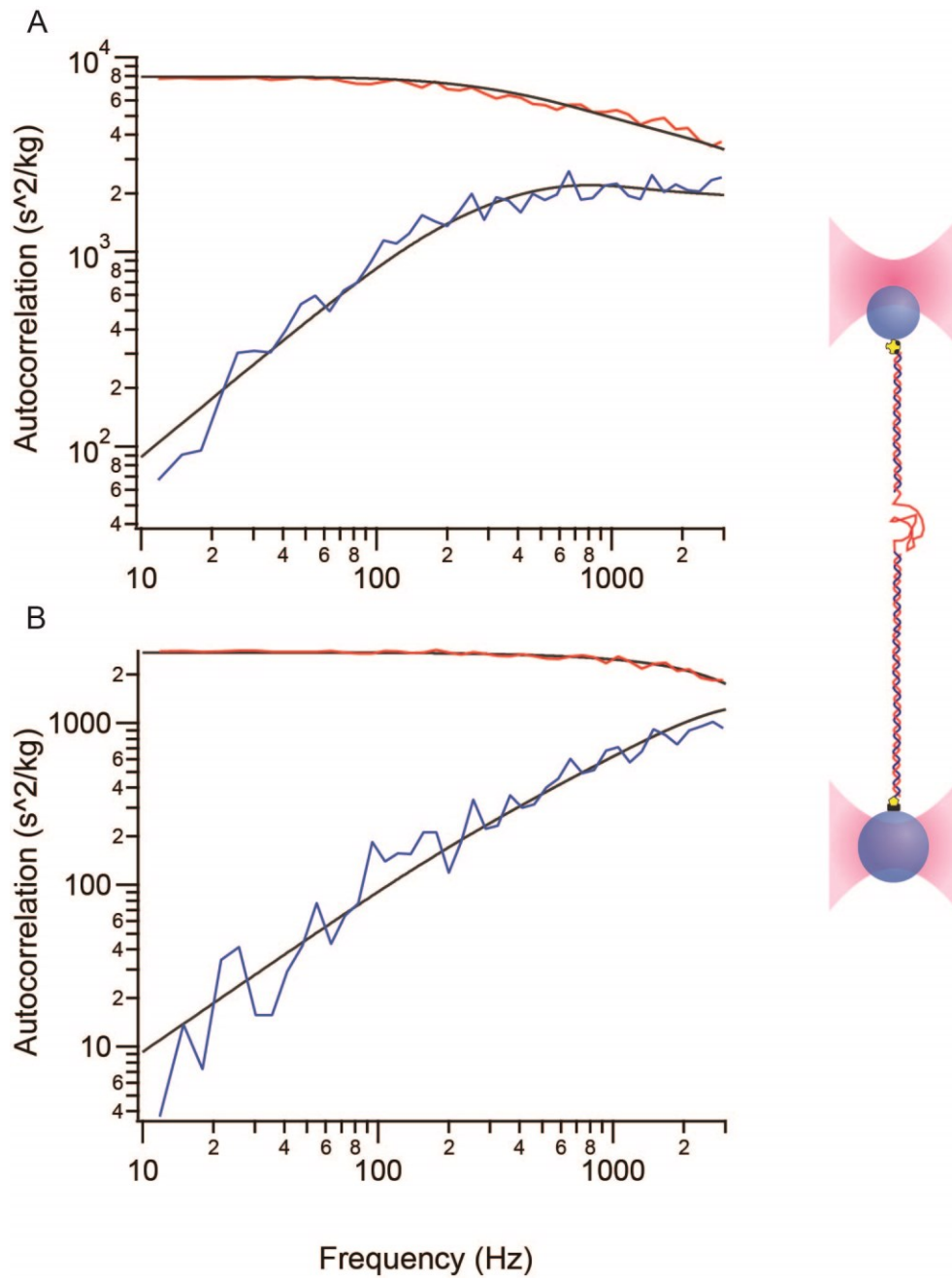


Figure 5.11: The position autocorrelation of a construct with handles and protein being held at a constant force of 10.8 pN in the folded state. The corresponding frequency response of the (a) 300 nm bead operating in the zero-stiffness region of the trap (trap 1) (b) 410 nm bead operating in the linear region of the trap (trap 2). Black lines are the corresponding fit to the response functions using equation 5.12.

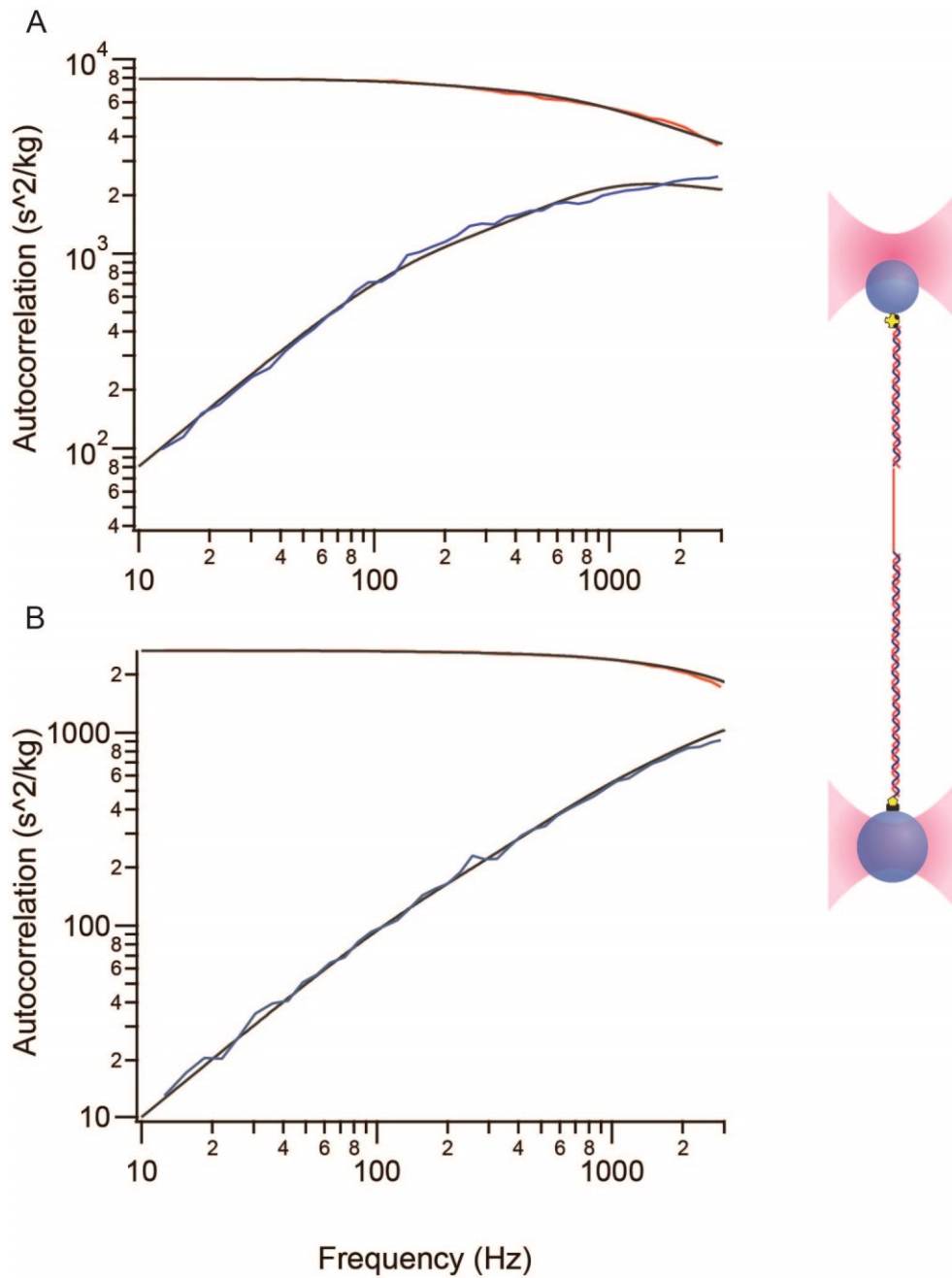


Figure 5.12: The position autocorrelation of a construct with handles and protein being held at a constant force of 10.8 pN in the unfolded state. The corresponding frequency response of the (a) 300 nm bead operating in the zero-stiffness region of the trap (trap 1) (b) 410 nm bead operating in the linear region of the trap (trap 2). Black lines are the corresponding fit to the response functions using equation 5.12.

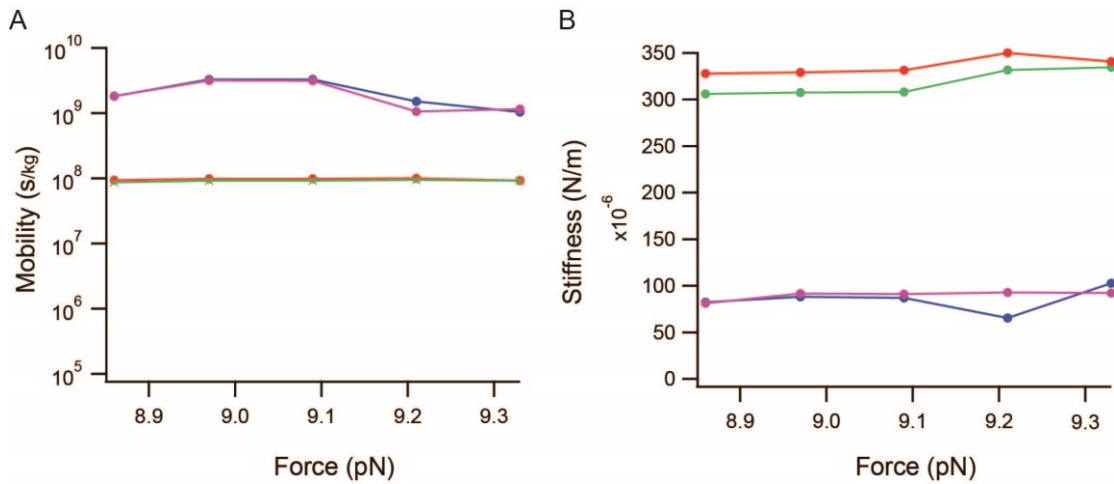


Figure 5.13: The extracted bead parameters. The 300 nm bead in trap 1 when the construct is in the unfolded (blue) and folded (purple) states. The 410 nm bead in trap 2 when the construct is in the unfolded (red) and folded (green) states.

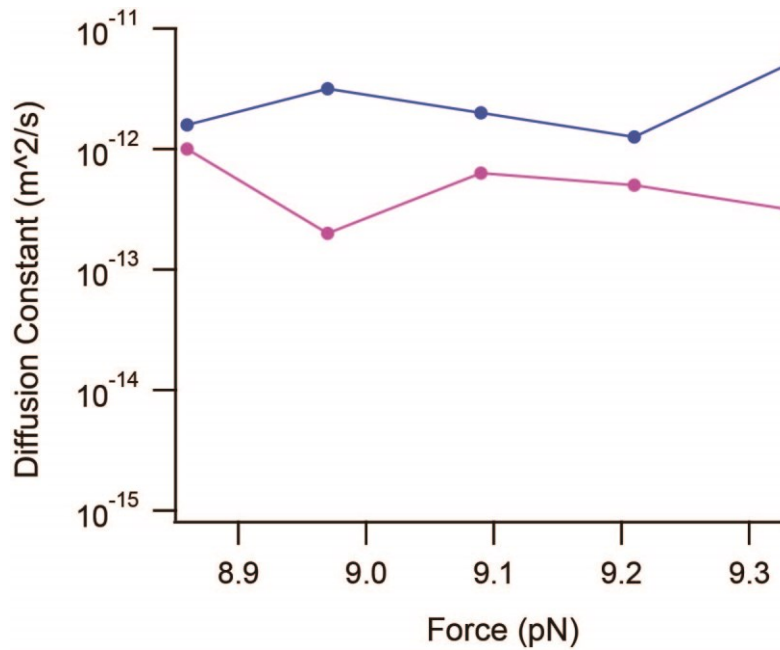


Figure 5.14: Diffusion coefficient calculated from the mobility of the protein (μ^P). Blue and purple lines are the diffusion coefficient for the unfolded and folded states, respectively.

Based on the above results, we can conclude that the dynamic deconvolution theory is indeed capable of capturing a protein conformational dynamics. The fact that the extracted diffusion coefficient of the energy landscape agrees with previously reported values suggest that this theory is viable, provided further revisions can be made to address the limitations illustrated in the previous sections.

6 Conclusion and Future Work

In this thesis, we demonstrated how the conformational dynamics of a molecule can be probed by utilizing various measurement modes of optical tweezers. We also presented different data analysis methods that are able to recover important energy landscape parameters, such as the diffusion coefficient, free energy and rates.

6.1 RNA pseudoknot conformational dynamics

The role of mRNA conformational plasticity in -1 PRF could be probed further by extending this kind of study to other stimulatory structures. For example, in the case of HIV-1, -1 PRF is apparently stimulated by a hairpin with a 3-nt bulge (Staple and Butcher, 2005). The local stability of the three base-pairs adjacent to the ribosomal RNA entry tunnel is known to influence -1 PRF efficiency (Marcheschi et al., 2011), but the structural dynamics of the hairpin have yet to be explored as a determining factor. Furthermore, the HIV-1 stimulatory structure may actually form an intramolecular triplex during -1 PRF (Dinman et al., 2002), raising structural parallels with pseudoknot-induced frameshifting. Ligands that modulate -1 PRF efficiency in HIV-1 (Brakier-Gingras et al., 2012; Marcheschi et al., 2011) would provide an opportunity to probe the link between conformational dynamics and -1 PRF in a different system and thereby test the generality of the proposed mechanism.

Finally, we note that our results suggest that when screening for molecules with potential as anti-viral therapeutics that work by modulating -1 PRF efficiency, focusing on the effects of compounds on pseudoknot conformational dynamics should prove more fruitful than focusing simply on modulating the stability of the pseudoknot structure. A similar strategy may also prove effective for targeting -1 PRF stimulated by other types of structures, like the hairpin in the HIV-1 frameshift signal.

6.2 Dynamic Deconvolution Theory

The dynamic deconvolution theory presented in chapter 4 and 5 is interesting, but it is far from complete. We showed how we can build up the network by incorporating elements in sequence, and consequently verified by experiments. We tested the validity of the bead response function, although it is found to be limited to a certain frequency range. The high frequency discrepancy suggests that there is some unknown interference, most likely arising from instrumental effects that contribute to the autocorrelation of the bead position.

Although the experimental results look promising, we can further improve our measurement protocols. For example, constant force measurements can be done in a more systematic way by measuring the bead-only movements after the construct breaks. This will allow us to extract the bead mobility under the same experiment conditions, reducing the parameter list by another four (two for each bead). On the other hand, the DNA measurement can be repeated with handles of different length.

For future work, we would like to test the theory on other molecules, such as those with more than two states. We wish to apply this theory, if successfully validated, to study the difference between an on or off pathway intermediate states. The dynamic deconvolution of network promises an alternative way of understanding a molecule's conformational dynamics by extracting the diffusion coefficient of each extension state.

References

- Ahn, D.-G., Lee, W., Choi, J.-K., Kim, S.-J., Plant, E.P., Almazán, F., Taylor, D.R., Enjuanes, L., and Oh, J.-W. (2011). Interference of ribosomal frameshifting by antisense peptide nucleic acids suppresses SARS coronavirus replication. *Antiviral Res.* *91*, 1–10.
- Anfinsen, C.B. (1973). Principles that Govern the Folding of Protein Chains. *Science* *181*, 223–230.
- Ashkin, A. (1970). Acceleration and Trapping of Particles by Radiation Pressure. *Phys. Rev. Lett.* *24*, 156–159.
- Ashkin, A. (2000). History of optical trapping and manipulation of small-neutral particle, atoms, and molecules. *IEEE Journal of Selected Topics in Quantum Electronics* *6*, 841–856.
- Ashkin, A., Dziedzic, J.M., Bjorkholm, J.E., and Chu, S. (1986). Observation of a single-beam gradient force optical trap for dielectric particles. *Opt. Lett.* *11*, 288–290.
- Baranov, P.V., Henderson, C.M., Anderson, C.B., Gesteland, R.F., Atkins, J.F., and Howard, M.T. (2005). Programmed ribosomal frameshifting in decoding the SARS-CoV genome. *Virology* *332*, 498–510.
- Bell, G.I. (1978). Models for the specific adhesion of cells to cells. *Science* *200*, 618–627.
- Berg-Sørensen, K., and Flyvbjerg, H. (2004). Power spectrum analysis for optical tweezers. *Review of Scientific Instruments* *75*, 594–612.
- Berkovich, R., Hermans, R.I., Popa, I., Stirnemann, G., Garcia-Manyes, S., Berne, B.J., and Fernandez, J.M. (2012). Rate limit of protein elastic response is tether dependent. *PNAS*.
- Brakier-Gingras, L., Charbonneau, J., and Butcher, S.E. (2012). Targeting frameshifting in the human immunodeficiency virus. *Expert Opin. Ther. Targets* *16*, 249–258.
- Brierley, I., Gilbert, R.J.C., and Pennell, S. (2010). Pseudoknot-Dependent Programmed —1 Ribosomal Frameshifting: Structures, Mechanisms and Models. In *Recoding: Expansion of Decoding Rules Enriches Gene Expression*, J.F. Atkins, and R.F. Gesteland, eds. (Springer New York), pp. 149–174.
- Bryngelson, J.D., and Wolynes, P.G. (1987). Spin glasses and the statistical mechanics of protein folding. *PNAS* *84*, 7524–7528.
- Bryngelson, J.D., and Wolynes, P.G. (1989). Intermediates and barrier crossing in a random energy model (with applications to protein folding). *J. Phys. Chem.* *93*, 6902–6915.

- Bryngelson, J.D., Onuchic, J.N., Socci, N.D., and Wolynes, P.G. (1995). Funnels, pathways, and the energy landscape of protein folding: A synthesis. *Proteins: Structure, Function, and Bioinformatics* *21*, 167–195.
- Chen, G., Chang, K.-Y., Chou, M.-Y., Bustamante, C., and Tinoco, I., Jr (2009). Triplex structures in an RNA pseudoknot enhance mechanical stability and increase efficiency of -1 ribosomal frameshifting. *Proc. Natl. Acad. Sci. U.S.A.* *106*, 12706–12711.
- Chen, X., Chamorro, M., Lee, S.I., Shen, L.X., Hines, J.V., Tinoco, I., Jr, and Varmus, H.E. (1995). Structural and functional studies of retroviral RNA pseudoknots involved in ribosomal frameshifting: nucleotides at the junction of the two stems are important for efficient ribosomal frameshifting. *EMBO J.* *14*, 842–852.
- Cohen, L. (1992). Convolution, filtering, linear systems, the Wiener-Khinchin theorem: generalizations. pp. 378–393.
- Cornish, P.V., Hennig, M., and Giedroc, D.P. (2005). A loop 2 cytidine-stem 1 minor groove interaction as a positive determinant for pseudoknot-stimulated -1 ribosomal frameshifting. *Proc. Natl. Acad. Sci. U.S.A.* *102*, 12694–12699.
- Crooks, G.E. (1999). The Entropy Production Fluctuation Theorem and the Nonequilibrium Work Relation for Free Energy Differences. *Physical Review E* *60*, 2721–2726.
- Danilowicz, C., Greenfield, D., and Prentiss, M. (2005). Dissociation of Ligand–Receptor Complexes Using Magnetic Tweezers. *Anal. Chem.* *77*, 3023–3028.
- Dill, K.A., and Chan, H.S. (1997). From Levinthal to pathways to funnels. *Nat Struct Mol Biol* *4*, 10–19.
- Dinman, J.D., and Wickner, R.B. (1992). Ribosomal frameshifting efficiency and gag/gag-pol ratio are critical for yeast M1 double-stranded RNA virus propagation. *J. Virol.* *66*, 3669–3676.
- Dinman, J.D., Richter, S., Plant, E.P., Taylor, R.C., Hammell, A.B., and Rana, T.M. (2002). The frameshift signal of HIV-1 involves a potential intramolecular triplex RNA structure. *Proc. Natl. Acad. Sci. U.S.A.* *99*, 5331–5336.
- Dudko, O.K., Hummer, G., and Szabo, A. (2006). Intrinsic Rates and Activation Free Energies from Single-Molecule Pulling Experiments. *Phys. Rev. Lett.* *96*, 108101.
- Dudko, O.K., Hummer, G., and Szabo, A. (2008). Theory, analysis, and interpretation of single-molecule force spectroscopy experiments. *PNAS* *105*, 15755–15760.
- Dudko, O.K., Graham, T.G.W., and Best, R.B. (2011). Locating the Barrier for Folding of Single Molecules under an External Force. *Phys. Rev. Lett.* *107*, 208301.

- Dulude, D., Berchiche, Y.A., Gendron, K., Brakier-Gingras, L., and Heveker, N. (2006). Decreasing the frameshift efficiency translates into an equivalent reduction of the replication of the human immunodeficiency virus type 1. *Virology* 345, 127–136.
- Evans, E., and Ritchie, K. (1997). Dynamic strength of molecular adhesion bonds. *Biophys J* 72, 1541–1555.
- Frieda, K.L., and Block, S.M. (2012). Direct Observation of Cotranscriptional Folding in an Adenine Riboswitch. *Science* 338, 397–400.
- Giedroc, D.P., and Cornish, P.V. (2009). Frameshifting RNA pseudoknots: structure and mechanism. *Virus Res.* 139, 193–208.
- Green, L., Kim, C.-H., Bustamante, C., and Tinoco, I., Jr (2008). Characterization of the mechanical unfolding of RNA pseudoknots. *J. Mol. Biol.* 375, 511–528.
- Greenleaf, W.J., Woodside, M.T., Abbondanzieri, E.A., and Block, S.M. (2005). Passive All-Optical Force Clamp for High-Resolution Laser Trapping. *Phys. Rev. Lett.* 95, 208102.
- Greenleaf, W.J., Woodside, M.T., and Block, S.M. (2007). High-resolution, single-molecule measurements of biomolecular motion. *Annu Rev Biophys Biomol Struct* 36, 171–190.
- Greenleaf, W.J., Frieda, K.L., Foster, D.A.N., Woodside, M.T., and Block, S.M. (2008). Direct observation of hierarchical folding in single riboswitch aptamers. *Science* 319, 630–633.
- Gupta, A.N., Vincent, A., Neupane, K., Yu, H., Wang, F., and Woodside, M.T. (2011). Experimental validation of free-energy-landscape reconstruction from non-equilibrium single-molecule force spectroscopy measurements. *Nat Phys* 7, 631–634.
- Hansen, T.M., Reihani, S.N.S., Oddershede, L.B., and Sørensen, M.A. (2007). Correlation between mechanical strength of messenger RNA pseudoknots and ribosomal frameshifting. *Proc. Natl. Acad. Sci. U.S.A.* 104, 5830–5835.
- Harada, Y., and Asakura, T. (1996). Radiation forces on a dielectric sphere in the Rayleigh scattering regime. *Optics Communications* 124, 529–541.
- Hinczewski, M., Hansen, Y. von, and Netz, R.R. (2010). Deconvolution of dynamic mechanical networks. *PNAS* 107, 21493–21498.
- Hoffmann, A., and Woodside, M.T. (2011). Signal-Pair Correlation Analysis of Single-Molecule Trajectories. *Angewandte Chemie International Edition* 50, 12643–12646.
- Houck-Loomis, B., Durney, M.A., Salguero, C., Shankar, N., Nagle, J.M., Goff, S.P., and D'Souza, V.M. (2011). An equilibrium-dependent retroviral mRNA switch regulates translational recoding. *Nature* 480, 561–564.

- Hummer, G., and Szabo, A. (2001). Free energy reconstruction from nonequilibrium single-molecule pulling experiments. *PNAS* *98*, 3658–3661.
- Jacks, T., Madhani, H.D., Masiarz, F.R., and Varmus, H.E. (1988). Signals for ribosomal frameshifting in the Rous sarcoma virus gag-pol region. *Cell* *55*, 447–458.
- Jarzynski, C. (1997). Nonequilibrium Equality for Free Energy Differences. *Phys. Rev. Lett.* *78*, 2690–2693.
- Kang, H., Hines, J.V., and Tinoco, I., Jr (1996). Conformation of a non-frameshifting RNA pseudoknot from mouse mammary tumor virus. *J. Mol. Biol.* *259*, 135–147.
- Kim, Y.G., Su, L., Maas, S., O'Neill, A., and Rich, A. (1999). Specific mutations in a viral RNA pseudoknot drastically change ribosomal frameshifting efficiency. *Proc. Natl. Acad. Sci. U.S.A.* *96*, 14234–14239.
- Kontos, H., Naphine, S., and Brierley, I. (2001). Ribosomal pausing at a frameshifter RNA pseudoknot is sensitive to reading phase but shows little correlation with frameshift efficiency. *Mol. Cell. Biol.* *21*, 8657–8670.
- Koshland, D.E. (1995). The Key–Lock Theory and the Induced Fit Theory. *Angewandte Chemie International Edition in English* *33*, 2375–2378.
- Landau, L.D., and Lifshitz, E.M. (1996). *Statistical Physics* (Elsevier).
- Lannon, H., Haghpanah, J.S., Montclare, J.K., Vanden-Eijnden, E., and Brujic, J. (2013). Force-Clamp Experiments Reveal the Free-Energy Profile and Diffusion Coefficient of the Collapse of Protein Molecules. *Phys. Rev. Lett.* *110*, 128301.
- Lee, G.U., Kidwell, D.A., and Colton, R.J. (1994). Sensing Discrete Streptavidin-Biotin Interactions with Atomic Force Microscopy. *Langmuir* *10*, 354–357.
- Leopold, P.E., Montal, M., and Onuchic, J.N. (1992). Protein folding funnels: a kinetic approach to the sequence-structure relationship. *PNAS* *89*, 8721–8725.
- Levinthal, C. (1968). Are there pathways for protein folding. *J. Chim. Phys* *65*, 44–45.
- Liphardt, J., Naphine, S., Kontos, H., and Brierley, I. (1999). Evidence for an RNA pseudoknot loop-helix interaction essential for efficient -1 ribosomal frameshifting. *J. Mol. Biol.* *288*, 321–335.
- Liphardt, J., Onoa, B., Smith, S.B., Tinoco, I., and Bustamante, C. (2001). Reversible Unfolding of Single RNA Molecules by Mechanical Force. *Science* *292*, 733–737.
- Marcheschi, R.J., Tonelli, M., Kumar, A., and Butcher, S.E. (2011). Structure of the HIV-1 frameshift site RNA bound to a small molecule inhibitor of viral replication. *ACS Chem. Biol.* *6*, 857–864.
- Marko, J.F., and Siggia, E.D. (1995). Stretching DNA. *Macromolecules* *28*, 8759–8770.

- Mosconi, F., Allemand, J.F., Bensimon, D., and Croquette, V. (2009). Measurement of the Torque on a Single Stretched and Twisted DNA Using Magnetic Tweezers. *Phys. Rev. Lett.* *102*, 078301.
- Namy, O., Moran, S.J., Stuart, D.I., Gilbert, R.J.C., and Brierley, I. (2006). A mechanical explanation of RNA pseudoknot function in programmed ribosomal frameshifting. *Nature* *441*, 244–247.
- Napthine, S., Liphardt, J., Bloys, A., Routledge, S., and Brierley, I. (1999). The role of RNA pseudoknot stem 1 length in the promotion of efficient -1 ribosomal frameshifting. *J. Mol. Biol.* *288*, 305–320.
- Nelson, D.D.L., Lehninger, A.L., and Cox, M.M. (2013). *Lehninger Principles of Biochemistry* (W.H. Freeman).
- Neuman, K.C., and Nagy, A. (2008). Single-molecule force spectroscopy: optical tweezers, magnetic tweezers and atomic force microscopy. *Nat Meth* *5*, 491–505.
- Neuman, K.C., Lionnet, T., and Allemand, J.-F. (2007). Single-Molecule Micromanipulation Techniques. *Annual Review of Materials Research* *37*, 33–67.
- Neupane, K., Yu, H., Foster, D.A.N., Wang, F., and Woodside, M.T. (2011). Single-molecule force spectroscopy of the add adenine riboswitch relates folding to regulatory mechanism. *Nucleic Acids Res.* *39*, 7677–7687.
- Olsthoorn, R.C.L., Reumerman, R., Hilbers, C.W., Pleij, C.W.A., and Heus, H.A. (2010). Functional analysis of the SRV-1 RNA frameshifting pseudoknot. *Nucleic Acids Res.* *38*, 7665–7672.
- Park, S.-J., Kim, Y.-G., and Park, H.-J. (2011). Identification of RNA pseudoknot-binding ligand that inhibits the -1 ribosomal frameshifting of SARS-coronavirus by structure-based virtual screening. *J. Am. Chem. Soc.* *133*, 10094–10100.
- Pathria, R.K., and Beale, P.D. (2011). *Statistical mechanics* (Amsterdam [u.a.]: Elsevier).
- Plant, E.P., and Dinman, J.D. (2005). Torsional restraint: a new twist on frameshifting pseudoknots. *Nucleic Acids Res.* *33*, 1825–1833.
- Plant, E.P., Jacobs, K.L.M., Harger, J.W., Meskauskas, A., Jacobs, J.L., Baxter, J.L., Petrov, A.N., and Dinman, J.D. (2003). The 9-A solution: how mRNA pseudoknots promote efficient programmed -1 ribosomal frameshifting. *RNA* *9*, 168–174.
- Plant, E.P., Pérez-Alvarado, G.C., Jacobs, J.L., Mukhopadhyay, B., Hennig, M., and Dinman, J.D. (2005). A three-stemmed mRNA pseudoknot in the SARS coronavirus frameshift signal. *PLoS Biol.* *3*, e172.
- Plant, E.P., Rakauskaitė, R., Taylor, D.R., and Dinman, J.D. (2010). Achieving a golden mean: mechanisms by which coronaviruses ensure synthesis of the correct stoichiometric ratios of viral proteins. *J. Virol.* *84*, 4330–4340.

- Plant, E.P., Sims, A.C., Baric, R.S., Dinman, J.D., and Taylor, D.R. (2013). Altering SARS coronavirus frameshift efficiency affects genomic and subgenomic RNA production. *Viruses* 5, 279–294.
- Qu, X., Wen, J.-D., Lancaster, L., Noller, H.F., Bustamante, C., and Tinoco, I., Jr (2011). The ribosome uses two active mechanisms to unwind messenger RNA during translation. *Nature* 475, 118–121.
- Rief, M., Oesterhelt, F., Heymann, B., and Gaub, H.E. (1997). Single Molecule Force Spectroscopy on Polysaccharides by Atomic Force Microscopy. *Science* 275, 1295–1297.
- Rief, M., Gautel, M., Schemmel, A., and Gaub, H.E. (1998). The Mechanical Stability of Immunoglobulin and Fibronectin III Domains in the Muscle Protein Titin Measured by Atomic Force Microscopy. *Biophysical Journal* 75, 3008–3014.
- Ritchie, D.B., Foster, D.A.N., and Woodside, M.T. (2012). Programmed –1 frameshifting efficiency correlates with RNA pseudoknot conformational plasticity, not resistance to mechanical unfolding. *PNAS* 109, 16167–16172.
- Ritchie, D.B., Soong, J., Sikkema, W.K.A., and Woodside, M.T. (2014). Anti-frameshifting Ligand Reduces the Conformational Plasticity of the SARS Virus Pseudoknot. *J. Am. Chem. Soc.* 136, 2196–2199.
- Serganov, A., and Patel, D.J. (2012). Metabolite recognition principles and molecular mechanisms underlying riboswitch function. *Annu Rev Biophys* 41, 343–370.
- Shehu-Xhilaga, M., Crowe, S.M., and Mak, J. (2001). Maintenance of the Gag/Gag-Pol ratio is important for human immunodeficiency virus type 1 RNA dimerization and viral infectivity. *J. Virol.* 75, 1834–1841.
- Shen, L.X., and Tinoco, I., Jr (1995). The structure of an RNA pseudoknot that causes efficient frameshifting in mouse mammary tumor virus. *J. Mol. Biol.* 247, 963–978.
- Smith, J.O. (2007). *Mathematics of the Discrete Fourier Transform (DFT): With Audio Applications* (Julius Smith).
- Staple, D.W., and Butcher, S.E. (2005). Solution structure and thermodynamic investigation of the HIV-1 frameshift inducing element. *J. Mol. Biol.* 349, 1011–1023.
- Su, M.-C., Chang, C.-T., Chu, C.-H., Tsai, C.-H., and Chang, K.-Y. (2005). An atypical RNA pseudoknot stimulator and an upstream attenuation signal for –1 ribosomal frameshifting of SARS coronavirus. *Nucleic Acids Res.* 33, 4265–4275.
- Telenti, A., Martinez, R., Munoz, M., Bleiber, G., Greub, G., Sanglard, D., and Peters, S. (2002). Analysis of Natural Variants of the Human Immunodeficiency Virus Type 1 gag-pol Frameshift Stem-Loop Structure. *J. Virol.* 76, 7868–7873.

- Thiel, V., Ivanov, K.A., Putics, A., Hertzog, T., Schelle, B., Bayer, S., Weissbrich, B., Snijder, E.J., Rabenau, H., Doerr, H.W., et al. (2003). Mechanisms and enzymes involved in SARS coronavirus genome expression. *J. Gen. Virol.* *84*, 2305–2315.
- Viana, N.B., Rocha, M.S., Mesquita, O.N., Mazolli, A., Maia Neto, P.A., and Nussenzveig, H.M. (2007). Towards absolute calibration of optical tweezers. *Phys. Rev. E* *75*, 021914.
- Waldauer, S.A., Bakajin, O., and Lapidus, L.J. (2010). Extremely slow intramolecular diffusion in unfolded protein L. *PNAS*.
- Wang, Y., Wills, N.M., Du, Z., Rangan, A., Atkins, J.F., Gesteland, R.F., and Hoffman, D.W. (2002). Comparative studies of frameshifting and nonframeshifting RNA pseudoknots: a mutational and NMR investigation of pseudoknots derived from the bacteriophage T2 gene 32 mRNA and the retroviral gag-pro frameshift site. *RNA* *8*, 981–996.
- Weiss, S. (1999). Fluorescence Spectroscopy of Single Biomolecules. *Science* *283*, 1676–1683.
- Yu, H., Liu, X., Neupane, K., Gupta, A.N., Brigley, A.M., Solanki, A., Sosova, I., and Woodside, M.T. (2012). Direct observation of multiple misfolding pathways in a single prion protein molecule. *PNAS* *109*, 5283–5288.
- Yu, H., Dee, D.R., and Woodside, M.T. (2013). Single-molecule approaches to prion protein misfolding. *Prion* *7*, 140–146.
- Zlatanova, J., and Leuba, S.H. (2003). Magnetic tweezers: a sensitive tool to study DNA and chromatin at the single-molecule level. *Biochem. Cell Biol.* *81*, 151–159.
- Zwanzig, R. (1988). Diffusion in a rough potential. *PNAS* *85*, 2029–2030.